

Materials Reliability Program: Technical Basis for Primary Water Stress Corrosion Cracking Mitigation by Surface Stress Improvement (MRP-267, Revision 1)

2012 TECHNICAL REPORT

Materials Reliability Program: Technical Basis for Primary Water Stress Corrosion Cracking Mitigation by Surface Stress Improvement (MRP-267, Revision 1)

1025839

Final Report, July 2012

EPRI Project Managers
P. Crooker
T. Lian

This document does **NOT** meet the requirements of
10CFR50 Appendix B, 10CFR Part 21,
ANSI N45.2-1977 and/or the intent of ISO-9001 (1994)

DISCLAIMER OF WARRANTIES AND LIMITATION OF LIABILITIES

THIS DOCUMENT WAS PREPARED BY THE ORGANIZATION(S) NAMED BELOW AS AN ACCOUNT OF WORK SPONSORED OR COSPONSORED BY THE ELECTRIC POWER RESEARCH INSTITUTE, INC. (EPRI). NEITHER EPRI, ANY MEMBER OF EPRI, ANY COSPONSOR, THE ORGANIZATION(S) BELOW, NOR ANY PERSON ACTING ON BEHALF OF ANY OF THEM:

(A) MAKES ANY WARRANTY OR REPRESENTATION WHATSOEVER, EXPRESS OR IMPLIED, (I) WITH RESPECT TO THE USE OF ANY INFORMATION, APPARATUS, METHOD, PROCESS, OR SIMILAR ITEM DISCLOSED IN THIS DOCUMENT, INCLUDING MERCHANTABILITY AND FITNESS FOR A PARTICULAR PURPOSE, OR (II) THAT SUCH USE DOES NOT INFRINGE ON OR INTERFERE WITH PRIVATELY OWNED RIGHTS, INCLUDING ANY PARTY'S INTELLECTUAL PROPERTY, OR (III) THAT THIS DOCUMENT IS SUITABLE TO ANY PARTICULAR USER'S CIRCUMSTANCE; OR

(B) ASSUMES RESPONSIBILITY FOR ANY DAMAGES OR OTHER LIABILITY WHATSOEVER (INCLUDING ANY CONSEQUENTIAL DAMAGES, EVEN IF EPRI OR ANY EPRI REPRESENTATIVE HAS BEEN ADVISED OF THE POSSIBILITY OF SUCH DAMAGES) RESULTING FROM YOUR SELECTION OR USE OF THIS DOCUMENT OR ANY INFORMATION, APPARATUS, METHOD, PROCESS, OR SIMILAR ITEM DISCLOSED IN THIS DOCUMENT.

REFERENCE HEREIN TO ANY SPECIFIC COMMERCIAL PRODUCT, PROCESS, OR SERVICE BY ITS TRADE NAME, TRADEMARK, MANUFACTURER, OR OTHERWISE, DOES NOT NECESSARILY CONSTITUTE OR IMPLY ITS ENDORSEMENT, RECOMMENDATION, OR FAVORING BY EPRI.

THE FOLLOWING ORGANIZATION(S), UNDER CONTRACT TO EPRI, PREPARED THIS REPORT:

Dominion Engineering, Inc.

Electric Power Research Institute (EPRI)

Hitachi-GE Nuclear Energy, Ltd.

Metal Improvement Company, LLC

Mitsubishi Heavy Industries, Ltd. and Mitsubishi Nuclear Energy Systems Inc.

Toshiba Corporation

AREVA NP, Inc.

Nuclear Research Institute

THE TECHNICAL CONTENTS OF THIS DOCUMENT WERE **NOT** PREPARED IN ACCORDANCE WITH THE EPRI QUALITY PROGRAM MANUAL (WHICH FULFILLS THE REQUIREMENTS OF 10 CFR 50, APPENDIX B AND 10 CFR 21, ANSI N45.2-1977 AND/OR THE INTENT OF ISO-9001 (1994)). USE OF THE CONTENTS OF THIS PRODUCT IN NUCLEAR SAFETY OR NUCLEAR QUALITY APPLICATIONS REQUIRES COMMERCIAL GRADE DEDICATION OR ADDITIONAL ACTIONS BY THE RECEIVING ORGANIZATIONS.

NOTE

For further information about EPRI, call the EPRI Customer Assistance Center at 800.313.3774 or e-mail askepri@epri.com.

Electric Power Research Institute, EPRI, and TOGETHER...SHAPING THE FUTURE OF ELECTRICITY are registered service marks of the Electric Power Research Institute, Inc.

Copyright © 2012 Electric Power Research Institute, Inc. All rights reserved.

ACKNOWLEDGMENTS

This report was prepared by

Dominion Engineering, Inc.
12100 Sunrise Valley Dr., Suite 220
Reston, VA 20191

Principal Investigator
G. White
I. Hamilton
J. Gorman

Electric Power Research Institute (EPRI)
1300 W.T. Harris Blvd.
Charlotte, NC 28262
Principal Investigator
T. Lian

Hitachi-GE Nuclear Energy, Ltd.
2-2, Omika-cho, 5-chome, Hitachi-shi
Ibaraki-ken, 319-1221 Japan
Principal Investigator
A. Kanno

Metal Improvement Company, LLC
7655 Longard Road
Livermore, CA 94551
Principal Investigator
L. Hackel

Mitsubishi Heavy Industries Ltd.
1-1-1 Wadasaki-cho Hyogo-ku
Kobe, Japan
Principal Investigator
K. Okimura

Toshiba Corporation
Isogo Nuclear Engineering Center
8, Shinsugita-cho, Isogo-ku
Yokohama 235-8523, Japan
Principal Investigator
M. Yoda

AREVA NP, Inc.
Tour AREVA
92084 Paris La Defense, France
Principal Investigator
I. de Curières

Nuclear Research Institute
Husinec-Rez cp 130, 250 68
Czech Republic
Principal Investigator
M. Postler

This report describes research sponsored by the EPRI.

The contributions of the MRP utility participants and EPRI consultants are gratefully acknowledged. The MRP utility participants and EPRI consultants included Gary Alkire (Exelon), Guy DeBoo (Exelon), Richard Gimple (Wolf Creek Nuclear Operating Corporation), Jamie GoBell (Entergy), Beth Haluska (Dominion Generation), Bernie Rudell (Constellation Energy Group), William Sims (Entergy), Dennis Weakland (Ironwood Consulting), and Tim Wells (Southern Nuclear).

The report is a corporate document that should be cited in the literature in the following manner:

Materials Reliability Program: Technical Basis for Primary Water Stress Corrosion Cracking Mitigation by Surface Stress Improvement (MRP-267, Revision 1), EPRI, Palo Alto, CA: 2012. 1025839.

PRODUCT DESCRIPTION

During the past two decades, stress corrosion cracking (SCC) has become the most relevant phenomenon affecting nuclear plant availability and plant lifetime management. SCC can lead to increased costs for operation, maintenance, assessment, repair, and replacement of boiling water reactor (BWR) and pressurized water reactor (PWR) components. Alloy 600 and 82/182 materials, which are widely used in PWR systems, are susceptible to primary water stress corrosion cracking (PWSCC). PWSCC has been reported in U.S. and international plants on reactor pressure vessel top head penetration nozzles (RPVHPNs), reactor vessel bottom-mounted nozzles (BMNs), and dissimilar metal welds (DMWs) of primary system piping as well as on other Alloy 600/82/182 pressure boundary components such as steam generator tubes and plugs, pressurizer heater sleeves, pressurizer instrumentation nozzles, and reactor hot-leg piping instrumentation nozzles.

Background

It is widely recognized that PWSCC susceptibility is strongly dependent on a combination of three factors: tensile surface stress, susceptible material, and the elevated temperature environment of PWR coolant. Therefore, PWSCC can be mitigated by removing one or more of those factors. This has led to development of various mitigation techniques, including surface stress improvement (SSI), weld overlay, weld in-lay, weld on-lay, and coolant chemical control.

This Materials Reliability Program (MRP) report focuses on the SSI techniques of laser peening (LP) and water jet peening (WJP), with coverage of field implementation issues and system design. Although the two LP processes—underwater laser peening (ULP) and air laser peening (ALP)—operate by the same physical principles, they are discussed separately because of significant differences in process parameters and equipment.

Objectives

This report establishes the technical basis for applying SSI treatments in mitigating PWSCC as a viable method to protect key PWR plant assets. Specific goals include the following:

- To determine the effectiveness of SSI treatments as alternative mitigation options to be applied in the nuclear industry
- To present information on implementing these SSI treatments that EPRI members can consider in pursuing proactive mitigation options
- To identify Alloy 600/82/182 locations for which relaxation of inspection requirements is appropriate after applying SSI mitigation treatments

Approach

Peening vendors and EPRI performed separate verification experiments—among them corrosion cracking and stress relaxation tests—to confirm the effectiveness and sustainability of SSI treatments in various environments, including a simulated PWR environment.

Results

To facilitate the implementation of SSI techniques as PWSCC mitigation methods, this report provides process information and experimental data supporting the effectiveness of the currently available LP and WJP processes. The intent is to provide alternative mitigation options for utilities addressing PWSCC concerns for PWR locations including RPVHPNs, BMNs, and DMW locations such as reactor vessel inlet/outlet nozzle welds.

The experimental results demonstrate that SSI treatments are effective measures in preventing or mitigating PWSCC, when performed in combination with an appropriate program of nondestructive examinations. When properly applied, SSI treatments—converting stress status from tension to compressive to a certain depth—can successfully eliminate the potential for future SCC initiation at surfaces exposed to reactor coolant. There are 13 years of LWR plant experience with actual ULP and WJP applications outside the United States, demonstrating that peening is a technically viable solution.

Applications, Value, and Use

Several technologies have been developed to address PWSCC, including mitigation methods such as weld overlay and mechanical stress improvement as well as component replacements using PWSCC-resistant materials. However, some Alloy 600/82/182 components cannot be mitigated by the current methods or economically replaced. Such components include RPVHPNs (control rod drive mechanism, control element drive mechanism, top head instrumentation, and head vent nozzles), BMNs, and some piping DMWs, in particular those with limited access at the pipe exterior. For these components, viable solutions are still needed to mitigate PWSCC, avoid costly replacements, and reduce the inspection burden. SSI is one such solution that has been implemented for SCC mitigation in dozens of BWR and PWR plants in Japan and other industries globally to address SCC and other degradation mechanisms.

Keywords

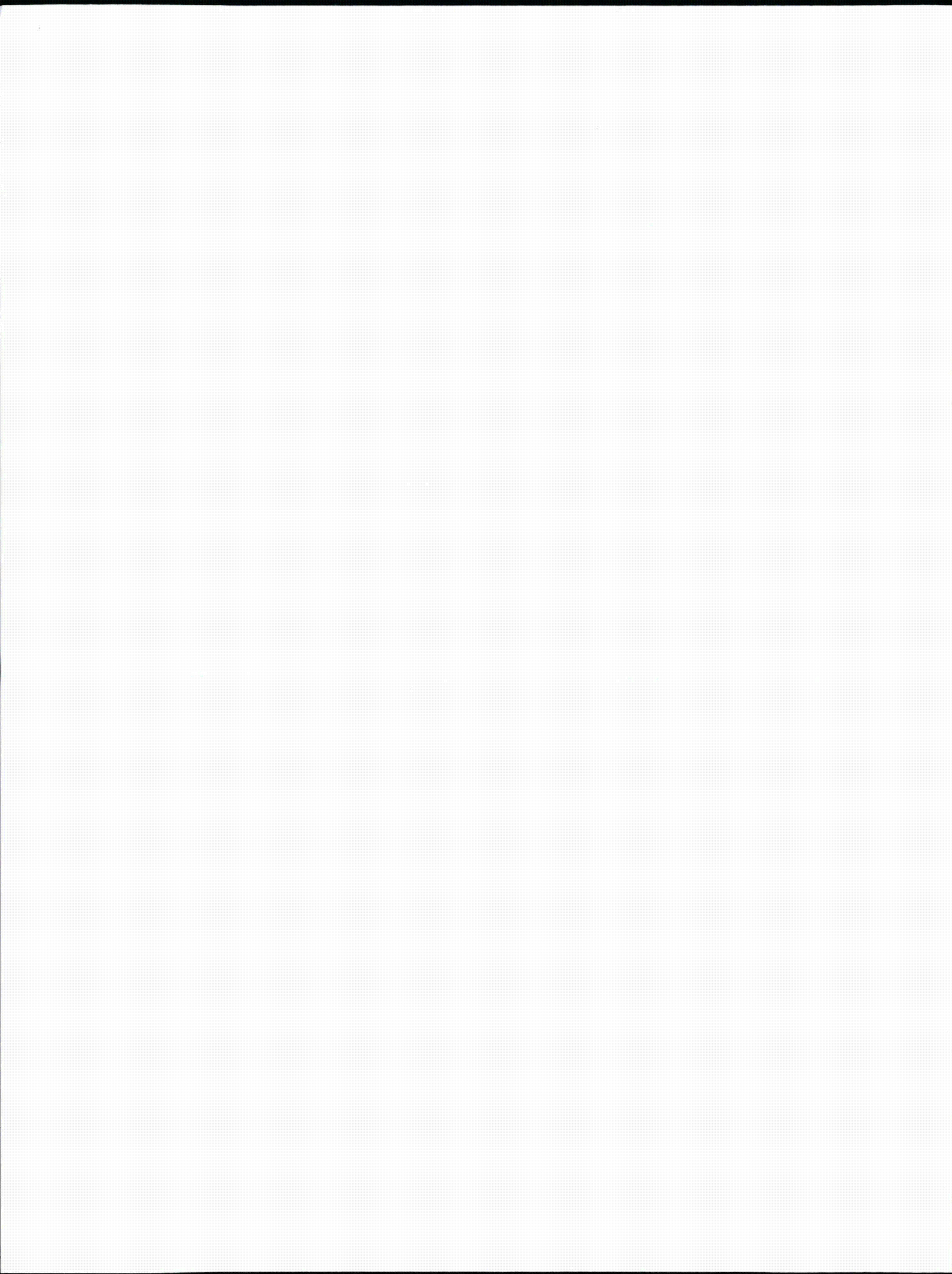
Crack mitigation
Laser peening (LP)
Laser shock peening (LSP)
Materials Reliability Program
Primary water stress corrosion cracking (PWSCC)
Surface stress improvement (SSI) techniques
Surface treatments
Water jet peening (WJP)

ABSTRACT

During the past two decades, stress corrosion cracking (SCC) has become the most relevant phenomenon affecting nuclear plant availability and plant lifetime management. SCC can lead to increased costs for operation, maintenance, assessment, repair, and replacement of boiling water reactor (BWR) and pressurized water reactor (PWR) components. Alloy 600 and 82/182 materials, which are widely used in PWR systems, are susceptible to primary water stress corrosion cracking (PWSCC). PWSCC has been reported in U.S. and international plants on reactor pressure vessel top head penetration nozzles (RPVHPNs), reactor vessel bottom mounted nozzles (BMNs), and dissimilar metal welds (DMWs) of primary system piping, as well as on other Alloy 600/82/182 pressure boundary components such as steam generator tubes and plugs, pressurizer heater sleeves, pressurizer instrumentation nozzles, and reactor hot-leg piping instrumentation nozzles.

It is widely recognized that PWSCC susceptibility is strongly dependent on a combination of three factors—tensile surface stress, susceptible material, and the elevated temperature environment of PWR coolant. Therefore, PWSCC can be mitigated by removing one or more of those three factors. This has led to application of various mitigation techniques, including surface stress improvement (SSI), weld overlay, weld in-lay, weld on-lay, and coolant chemical control.

This Materials Reliability Program (MRP) report focuses on the SSI treatment techniques of laser peening (LP) and water jet peening (WJP), with coverage of field implementation issues and system design. The experimental results demonstrate that SSI treatments are effective measures in preventing or mitigating PWSCC, when performed in combination with an appropriate program of non-destructive examinations. When properly applied, SSI treatments—converting stress status from tension to compressive to a certain depth—can successfully eliminate the potential for future SCC initiation at surfaces exposed to reactor coolant. Furthermore, there are 13 years of LWR plant experience with actual LP and WJP applications outside the U.S., demonstrating that peening is a technically viable solution.

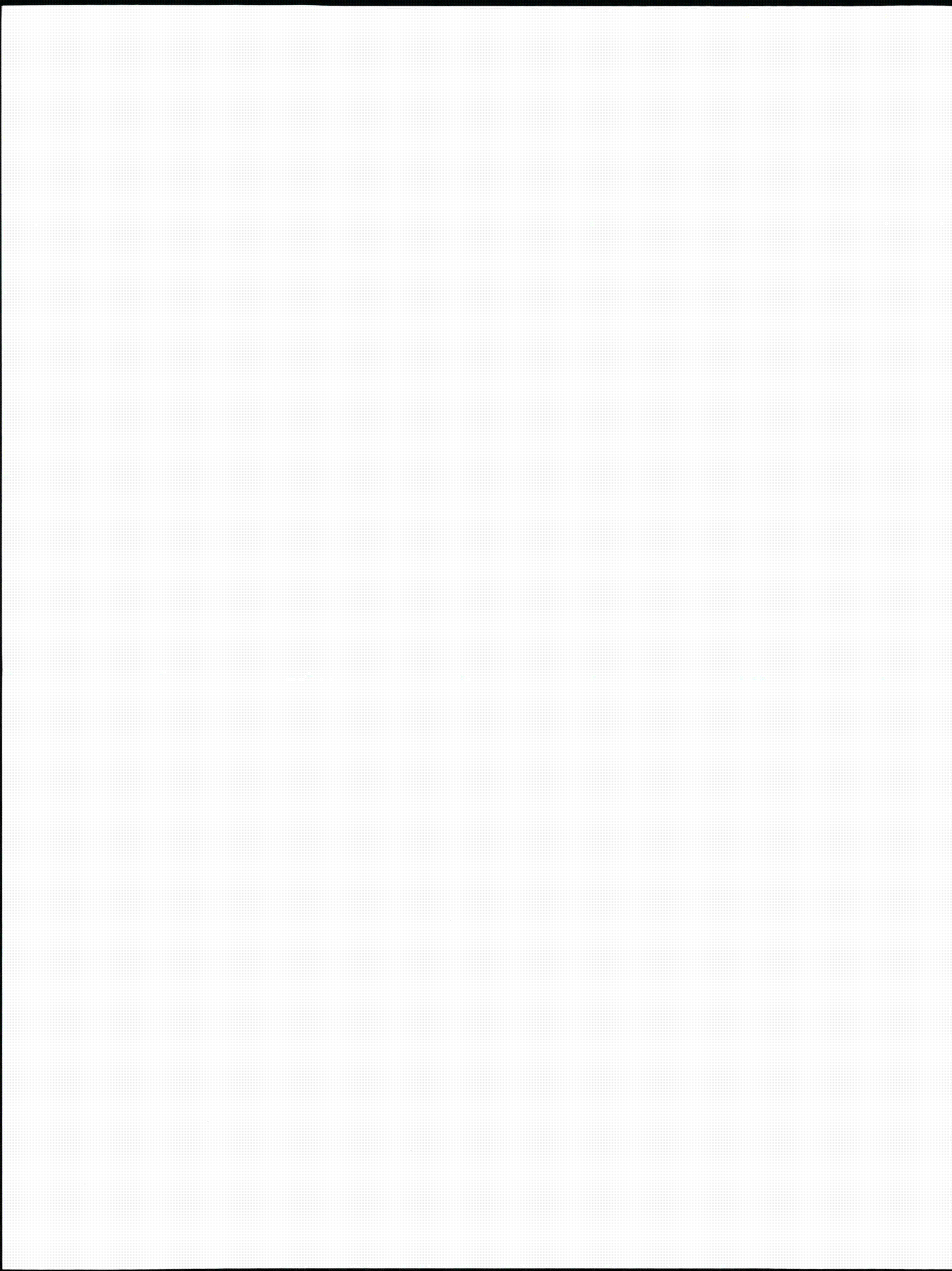


ACRONYMS

ABWR	Advanced Boiling Water Reactor
ALP	Air Laser Peening
ASME	American Society of Mechanical Engineers
BMI	Bottom Mounted Instrumentation
BMN	Bottom Mounted Nozzle
BWR	Boiling Water Reactor
CBB	Crevice Bent Beam
CEDM	Control Element Drive Mechanism
CRDM	Control Rod Drive Mechanism
CW	Continuous-Wave
DOF	Degree of Freedom
DMW	Dissimilar Metal Weld
EASA	European Aviation Safety Agency
EDY	Effective Degradation Year
EMC	Electromagnetic Compatibility
EPRI	Electric Power Research Institute
FAA	Federal Aviation Administration
FWHM	Full Width at Half Maximum
GE	General Electric
HAZ	Heat-Affected Zone
HGNE	Hitachi GE Nuclear Energy
ID	Inner Diameter
ICI	In-Core Instrumentation
IGSCC	Intergranular Stress Corrosion Cracking
IMI	Incore Monitoring Instrumentation
JANTI	Japan Nuclear Technology Institute

JAPEIC	Japan Power Engineering and Inspection Corporation
JSME	Japan Society of Mechanical Engineers
LLNL	Lawrence Livermore National Laboratory
LP	Laser Peening
LSP	Laser Shock Peening
LUT	Laser Ultrasonic Testing
LWR	Light Water Reactor
MIC	Metal Improvement Company
MHI	Mitsubishi Heavy Industries, Ltd.
MHV	Vickers Material Microhardness
MRP	Materials Reliability Program
NDE	Nondestructive Examination
NRC	US Nuclear Regulatory Commission
NRI	Nuclear Research Institute
OD	Outer Diameter
PLP	Portable Laser Peening
PRF	Pulse Repetition Frequency
PT	Dye-Penetrant Testing
PWR	Pressurized Water Reactor
PWSCC	Primary Water Stress Corrosion Cracking
RCS	Reactor Coolant System
RIY	Reinspection Year
RFO	Refueling Outage
RPV	Reactor Pressure Vessel
RUB	Reversed U-Bend
RV	Reactor Vessel
RPVHPN	Reactor Pressure Vessel (Top) Head Penetration Nozzle
SBS	Stimulated Brillouin Scattering
SCC	Stress Corrosion Cracking
SEM	Scanning Electron Microscope
SG	Steam Generator

SHG	Second Harmonic Generator
SMAW	Shielded Metal Arc Welding
SP	Shot Peening
SS	Stainless Steel
SSI	Surface Stress Improvement
ULP	Underwater Laser Peening
US	United States
USP	Ultrasonic Shot Peening
VT	Visual Testing
WJP	Water Jet Peening
XRD	X-Ray Diffraction



CONTENTS

1 INTRODUCTION	1-1
1.1 Background	1-1
1.1.1 Need Addressed by Surface Stress Improvement (SSI) Techniques.....	1-1
1.1.2 Commercialization of Underwater Laser Peening (ULP) and Water Jet Peening (WJP) Processes	1-2
1.1.3 Use of Underwater Laser Peening (ULP) and Water Jet Peening (WJP) in Japanese BWRs and PWRs.....	1-2
1.1.4 Commercialization of Air Laser Peening (ALP) Process	1-3
1.2 Purpose.....	1-3
1.3 Scope.....	1-4
1.4 Approach.....	1-4
1.5 Report Organization.....	1-5
2 THEORY AND TECHNOLOGY OF SURFACE STRESS IMPROVEMENT	2-1
2.1 Introduction	2-1
2.2 Underwater Laser Peening (ULP).....	2-2
2.2.1 ULP Surface Treatment Technologies and Principles of Operation	2-2
2.2.2 Numerical Analysis and Experimental Verification of ULP	2-3
2.2.2.1 Laser-Induced Plasma Pressure	2-4
2.2.2.2 Material Properties and Calculation System for Theoretical Analysis	2-5
2.2.2.3 Experimental Verification	2-7
2.2.2.4 Shock Wave Propagation and Residual Stress	2-9
2.3 Water Jet Peening (WJP)	2-10
2.3.1 Shock Waves During WJP	2-10
2.3.1.1 Cavitation Bubbles.....	2-10
2.3.1.2 Bubble Development and Collapse	2-11
2.3.2 WJP Surface Treatment Technologies and Principles of Operation	2-13
2.3.2.1 Nozzle Diameter	2-15
2.3.2.2 Nozzle Stand-Off	2-15

2.3.2.3	Water Jet to Material Angle	2-15
2.3.2.4	Flow Rate.....	2-16
2.3.2.5	Application Time	2-16
2.3.2.6	Thickness of the Materials to Be Mitigated	2-16
2.3.2.7	Water Pressure.....	2-16
2.4	Air Laser Peening (ALP)	2-17
2.4.1	Technology Introduction	2-17
2.4.2	Experimentally Measured Stress Profiles in ALP Treated Specimens	2-20
2.4.3	Current Commercial Applications of ALP	2-26
2.4.4	MIC Air Laser Peening (ALP) System	2-29
2.4.4.1	Beam characteristics	2-30
2.4.4.1.1	Pulse energy	2-30
2.4.4.1.2	Pulse width.....	2-31
2.4.4.1.3	Laser spot shape.....	2-31
2.4.4.1.4	Laser beam quality	2-32
2.4.4.2	Transportable laser.....	2-33
2.4.4.3	Beam transport	2-33
2.4.4.4	Scanning beam delivery head	2-33
2.4.4.5	Pattern registration	2-34
2.5	Summary.....	2-35
3	RELEVANT PLANT PEENING EXPERIENCE	3-1
3.1	Japanese PWR and BWR Peening Experience.....	3-1
3.1.1	Overview and Peening Methods Used in Japan.....	3-1
3.1.2	Development and Qualification.....	3-2
3.1.3	Process Controls	3-3
3.1.3.1	Underwater Laser Peening	3-3
3.1.3.2	Water Jet Peening	3-4
3.1.4	Service Experience	3-4
3.1.5	Inspection Methods and Results	3-5
3.2	Experience with Peening of Steam Generators	3-8
3.2.1	Introduction.....	3-8
3.2.2	Experience with OD Peening of Alloy 800 Tubes.....	3-9
3.2.3	Experience with ID Peening of Mill Annealed Alloy 600 (600MA) Tubes	3-11

3.2.4	Experience with ID Peening of Thermally Treated Alloy 600 (600TT) Tubes	3-11
3.2.5	Conclusions Regarding Peening of SG Tubes	3-12
3.3	Use of the Abrasive Water Jet Process	3-12
3.4	Application of Peening on Alloy 600 Pressurizer Heater Sheaths	3-13
3.5	Application of Peening to Alloy 718 Fuel Assembly Screws	3-13
4	EFFECTIVENESS OF SURFACE STRESS IMPROVEMENT	4-1
4.1	Effectiveness Criteria	4-1
4.2	Experimental Verification of Effectiveness of Surface Stress Improvement To Mitigate PWSCC	4-2
4.2.1	Residual Stress Measurements	4-2
4.2.2	Corrosion Cracking Tests	4-4
4.3	Long-Term Effectiveness of Surface Stress Improvement	4-5
4.3.1	Thermal Exposure Tests	4-6
4.3.2	Load Cycling Tests	4-6
4.4	Thermal Relaxation Calculation	4-7
4.4.1	Verification of the Activation Energy Range using the Zener-Wert-Avrami Function	4-7
4.4.2	Calculation of Equivalent Lifetime from Thermal Relaxation Experiments	4-12
4.4.3	Effects of Operating Stresses on Relaxation of Peening Induced Compressive Stresses	4-13
4.4.4	Summary	4-14
4.5	Verification of No Unacceptable Side Effects caused by Peening	4-14
4.6	Issues Related to Cold Work	4-16
4.6.1	Background Information – Cold Work vs. Hardness and Strength	4-16
4.6.2	Levels of Cold Work Developed by Peening	4-17
4.6.2.1	Hitachi-GE Water Jet Peening	4-17
4.6.2.2	MHI/MNES Water Jet Peening	4-18
4.6.2.3	Westinghouse – Toshiba Underwater Laser Peening	4-19
4.6.2.4	MIC Air Laser Peening	4-20
4.6.3	Effect of Cold Work from Peening on SCC and other Modes of Degradation	4-22
4.6.4	Effect of Prior Cold Work on Ability to Effectively Peen	4-22
4.6.5	Effect of Cold Work on Stress Relaxation	4-23
4.6.6	Effect of Cold Work on Phase Instability	4-24

4.7	Conclusions	4-24
5 IMPLEMENTATION CONSIDERATIONS OF LASER AND WATER JET PEENING TECHNIQUES		
5-1		5-1
5.1	Introduction	5-1
5.2	ULP System Development and Engineering Design.....	5-2
5.2.1	Control Strategy and Interlocks	5-2
5.2.2	Safety Strategy	5-3
5.2.3	ULP System Architecture	5-3
5.2.4	Other ULP Implementation Considerations	5-6
5.3	WJP System Development and Engineering Design	5-7
5.3.1	Control Parameters	5-8
5.3.2	Control Strategy and Interlocks	5-12
5.3.3	Safety Strategy	5-14
5.3.4	Other WJP Implementation Considerations	5-14
5.3.5	Typical Schedules	5-15
5.4	Application of ALP To Nuclear Power Plants	5-16
5.4.1	Development and Current Use of ALP Technology.....	5-16
5.4.2	Application to Nuclear Power Plants	5-16
5.4.3	Application to RPVHPNs	5-17
5.5	Conclusions	5-18
6 CONCLUSIONS AND RECOMMENDATIONS		
6-1		6-1
6.1	Key Conclusions	6-1
6.2	Recommendations	6-2
7 REFERENCES		
7-1		7-1
A EXPERIMENTAL VERIFICATION OF EFFECTIVENESS OF SURFACE STRESS IMPROVEMENT TO MITIGATE PWSCC.....		
A-1		A-1
A.1	Experimentally Measured Stress Results	A-2
A.1.1	Stress Measurements on Flat Plate Specimens.....	A-2
A.1.1.1	Flat Plates treated with ULP	A-2
A.1.1.2	Flat Plates treated with WJP.....	A-4
A.1.1.3	Flat Plates treated with ALP	A-13
A.1.2	Stress Analyses of Welded Plates.....	A-16

A.1.2.1	Welded Plates treated with ULP	A-16
A.1.2.2	Welded Plates treated with WJP	A-27
A.1.3	Stress Analyses of Underwater Laser Peened BMN-size Pipes and Mock-ups.....	A-32
A.1.3.1	BMN Size Pipes.....	A-32
A.1.3.2	BMN Mock ups	A-37
A.1.4	Reactor Mock up Experimentation performed by Hitachi-GE.....	A-39
A.1.5	Test Data on Peened ID BMN Mock-up performed by Mitsubishi	A-45
A.1.5.1	Description of BMN ID Mock-up Testing.....	A-45
A.1.5.2	Results of BMN ID Mock-up Testing.....	A-47
A.1.5.3	Discussion of BMN ID Mock-up Testing	A-55
A.1.6	Test Data on Peened OD/J-groove weld of a BMN Mock-up performed by Mitsubishi	A-55
A.1.6.1	Description of BMN OD/J-groove weld Mock-up Testing	A-55
A.1.6.2	Results of BMN OD/J-groove weld Mock-up Testing	A-58
A.1.6.3	Discussion of BMN OD/J-groove weld Mock-up Testing	A-65
A.1.7	Surface roughness measurements	A-66
A.1.8	Hardness measurements	A-70
A.1.9	Peening at extreme parameter values.....	A-77
A.2	SCC test data from vendors.....	A-79
A.2.1	SCC initiation test on specimens with no pre-existing flaws.....	A-79
A.2.2	Effects of peening to metal surface with pre-existing flaws	A-90
A.2.2.1	Evaluation of the impact of the application process to existing cracks	A-90
A.2.2.2	Effectiveness of peening in mitigating further growth of pre-existing SCC cracks.....	A-94
A.3	Independent testing to confirm the effectiveness of surface peening	A-103
A.3.1	Experimental Procedure.....	A-104
A.3.1.1	Test Material	A-104
A.3.1.2	Test Specimens	A-106
A.3.1.3	Test Environment and Duration	A-109
A.3.1.4	Modifications to Experimental Procedure in Phase 2	A-110
A.3.2	Surface Stress Improvement Mitigation Methods.....	A-111
A.3.2.1	Mitigation Methods examined in Phase 1	A-111
A.3.2.2	Mitigation Methods examined in Phase 2	A-112
A.3.3	Observations of U-Bend Surfaces before PWSCC Testing.....	A-113

A.3.3.1	U-Bend Pre-Peening Inspection for Experimentation Phase 1	A-113
A.3.3.2	U-Bend Pre-Peening Inspection for Experimentation Phase 2	A-114
A.3.4	Test Matrices	A-115
A.3.4.1	Test Matrix for Phase 1	A-115
A.3.4.2	Test Matrix for Phase 2	A-116
A.3.5	Results and Analysis	A-117
A.3.5.1	Phase 1 Surface Stresses and Cold Work of U-Bends	A-117
A.3.5.2	Phase 1 PWSCC Test Results	A-119
A.3.5.3	Surface Stresses and Cold Work of U-Bends in Phase 2	A-122
A.3.5.4	PWSCC Test Results in Phase 2	A-128
A.3.6	Discussion	A-136
A.3.6.1	Surface Stress Improvement Mitigation Methods	A-136
A.3.7	Summary and Perspectives	A-136
A.4	Experiments supporting No Unacceptable Side Effects from Peening	A-137
A.4.1	Effect of peening on inspectability by UT	A-137
A.4.2	Vibrational effect of WJP	A-138

B LONG-TERM EFFECTIVENESS OF SURFACE STRESS IMPROVEMENT..... B-1

B.1	Vendors' Tests on Sustainability	B-1
B.1.1	Sustainability of Stress Improvement by ULP	B-1
B.1.2	Sustainability of Stress Improvement by WJP	B-3
B.1.2.1	Stress Shakedown by Load Cycling	B-3
B.1.2.2	Thermal Stress Relaxation	B-8
B.2	Independent Testing by EPRI	B-12
B.2.1	Test Procedure	B-12
B.2.1.1	Autoclave and Test Parameters	B-13
B.2.1.2	Test Samples	B-15
B.2.1.3	Test Procedure	B-19
B.2.2	Test Results and Analysis	B-20
B.2.2.1	As-Manufactured Samples	B-20
B.2.2.2	Underwater Laser Peening by Toshiba	B-24
B.2.2.3	Water Jet Peening by Hitachi-GE	B-29
B.2.2.4	Water Jet Peening by Mitsubishi	B-33
B.2.2.5	Air Laser Peening by MIC	B-37
B.2.2.6	Comparison of Results across the four peening vendors	B-43

LIST OF FIGURES

Figure 2-1 PWSCC mitigation by surface treatment	2-1
Figure 2-2 Fundamental process of laser peening treatment, by Toshiba	2-3
Figure 2-3 Plasma generated by laser irradiation in air and in water, by Toshiba	2-4
Figure 2-4 One-dimensional model of laser-induced plasma, by Toshiba	2-5
Figure 2-5 Stress-strain relations of Type 304 stainless steel, by Toshiba	2-6
Figure 2-6 Finite element model for calculation of shock wave propagation, by Toshiba	2-6
Figure 2-7 Experimental setup of laser peening treatment, by Toshiba	2-7
Figure 2-8 Laser irradiation of a test sample immersed in water, by Toshiba	2-8
Figure 2-9 Test sample and scheme of laser irradiation, by Toshiba	2-8
Figure 2-10 Residual stress depth profile on Type 304 stainless steel with and without underwater laser peening, by Toshiba	2-9
Figure 2-11 Comparison between calculated and measured residual stress profiles, by Toshiba	2-10
Figure 2-12 Principle of WJP by submerged cavitating water jet, by Mitsubishi	2-14
Figure 2-13 Schematic diagrams and photos of the application of WJP to PWR components, by Mitsubishi	2-14
Figure 2-14 Schematic design of air laser peening process showing work piece, ablative layer, inertial tamping layer and laser input, provided by Metal Improvement Company (MIC)	2-17
Figure 2-15 Residual stress profiles as a function of depth for an aluminum alloy (Al 7050 T7451) treated with ALP and shot peening (SP), provided by MIC	2-19
Figure 2-16 Example of compressive residual stress profile for air laser peening of nickel-based Alloy 22, provided by MIC	2-19
Figure 2-17 Results of SCC testing performed with ALP on a butt weld geometry for Type 316 stainless steel material, provided by MIC	2-20
Figure 2-18 Residual stress versus depth as a function of number of peening layers in 20.8 mm thick coupons of nickel-based Alloy 22, provided by MIC	2-21
Figure 2-19 Residual stress profiles for ALP treatment of a nickel-based Alloy 22 weld, provided by MIC	2-22
Figure 2-20 Longitudinal component of residual stress at the center of the weld bead with and without air laser peening (Alloy 22), provided by MIC	2-23
Figure 2-21 Longitudinal component of residual stress at the right weld toe, with and without air laser peening (Alloy 22), provided by MIC	2-23
Figure 2-22 Longitudinal component of residual stress outside the weld region (30 mm from the weld center) with and without air laser peening (Alloy 22), provided by MIC	2-24

Figure 2-23 Difference between the longitudinal component of residual stress in air laser peened and unpeened weld samples, at various positions transverse to the weld (Alloy 22), provided by MIC	2-25
Figure 2-24 Residual stress versus depth as a function of number of peening layers in 9 mm thick coupons of nickel-based Alloy 22, provided by MIC	2-26
Figure 2-25 T-45 arrestment hook shank.....	2-27
Figure 2-26 Results of fatigue crack testing of unpeened, shot peened, and air laser peened T-45 arrestment-hook-shank-like samples, provided by MIC.....	2-28
Figure 2-27 Results of SCC tests of unpeened, shot peened, and air laser peened 300M steel C-ring coupons prepared according to ASTM G47-98, provided by MIC	2-29
Figure 2-28 Comparison of residual stress profiles for laser spot sizes ranging from 3 mm to 1 mm square at a fixed power density of 10 GW/cm ² (titanium alloy samples), provided by MIC	2-30
Figure 2-29 Comparison of laser output pulse shapes for widths of 9 to 27 ns, provided by MIC	2-31
Figure 2-30 Square spots allow complex surfaces on the work piece to be air laser peened with precisely controlled spot-to-spot overlap, provided by MIC	2-32
Figure 2-31 The MIC transportable air laser peening system: the figure on the left shows a schematic representation and the photo on the right shows a system in transit to Palmdale, CA to support on-site laser peening of F-22 aircraft, provided by MIC	2-33
Figure 2-32 Photo showing the MIC air laser peening stinger design which allows spot patterns to be placed over complex features of a stationary work piece, provided by MIC.....	2-34
Figure 3-1 Ultrasonic Shot Peening	3-2
Figure 3-2 Effect of Denting on Residual Stress and Susceptibility to ODSCC	3-10
Figure 4-1 Thermal relaxation of Alloy 182 and Type 316 L SS at 450°C for 1000 h provided by Hitachi-GE	4-9
Figure 4-2 Thermal Relaxation Data from Hitachi-GE for Alloy 600 plates treated with water jet peening and held at 450°C for 1000 h.....	4-10
Figure 4-3 Arrhenius plot for the first approach to thermal relaxation data treatment (based on data provided by Mitsubishi and Hitachi-GE)	4-10
Figure 4-4 Arrhenius plot for the second approach to thermal relaxation data treatment (based on data provided by Mitsubishi and Hitachi-GE)	4-11
Figure 4-5 Relationship between Cold Reduction, Hardness and Tensile Strength	4-17
Figure 4-6 Effects of Underwater Laser Peening on Hardness of Alloy 600, data provided by Toshiba.....	4-20
Figure 4-7 Residual Stress and Cold Work Distributions Developed in Alloy 718 Coupons Using Shot Peening, Gravity Peening and Air Laser Peening	4-21
Figure 5-1 Portable laser peening (PLP) system for inner surfaces of BMNs, by Toshiba.....	5-4
Figure 5-2 Portable laser peening (PLP) system for outer surfaces of BMNs, by Toshiba.....	5-5
Figure 5-3 Key support equipment for the ULP system, by Toshiba	5-6
Figure 5-4 Critical paths for ULP Application at Ikata Unit 1 and 2, by Toshiba	5-7
Figure 5-5 Essential variables of the WJP process to be controlled, by Hitachi-GE.....	5-8

Figure 5-6 Typical WJP system configuration in BWRs, by Hitachi-GE.....	5-9
Figure 5-7 WJP system for BMI nozzles, by MHI	5-10
Figure 5-8 WJP application equipment for BMI nozzles, by MHI	5-11
Figure 5-9 WJP application equipment for RPV Outlet/Inlet nozzles, by MHI	5-12
Figure 5-10 Examples of a custom-built WJP delivery tool, by Hitachi-GE.....	5-13
Figure 5-11 Control strategy of ensuring 100% treatment coverage, by Hitachi-GE	5-14
Figure 5-12 Transportable air laser peening system showing the output beam periscope and the first portion of the beam delivery pipes	5-18
Figure A-1 Comparison of cavitation (water jet), laser, and air laser peening on Alloy 600 flat plate specimens with selected parameters for each process (Figure 4-31 from MRP-162).....	A-2
Figure A-2 Residual stress depth profile of Alloy 600 and Alloy 132 plane specimens, by Toshiba	A-3
Figure A-3 Residual stress profiles on the surface and at depth for 304 stainless steel plate specimen treated with ULP by Toshiba	A-4
Figure A-4 The WJP partial mockup test facility, by Hitachi-GE	A-5
Figure A-5 Stress improvement with WJP (Alloy 600), by Hitachi-GE.....	A-6
Figure A-6 Stress improvement with WJP (Alloy 182), by Hitachi-GE.....	A-7
Figure A-7 Stress improvement with WJP (Type 304 SS), by Hitachi-GE.....	A-8
Figure A-8 Stress improvement with WJP (Type 316L SS), by Hitachi-GE.....	A-9
Figure A-9 Comparison of residual stress induced by WJP in stainless steel and nickel based alloys, provided by Hitachi-GE	A-10
Figure A-10 Residual surface stress profile of a 304 stainless steel plate peened with WJP by Hitachi-GE	A-11
Figure A-11 Residual stress profiles before and after WJP in a specimen with a pre- existing flaw, provided by Hitachi-GE.....	A-12
Figure A-12 Residual stress profiles before and after WJP in a specimen with multiple pre-existing cracks, provided by Hitachi-GE	A-13
Figure A-13 Surface stress measurements performed on an Alloy 600 specimen treated with ALP to assess edge effects	A-13
Figure A-14 Residual stress as a function of depth for Alloy 600 flat plates with various air laser peening treatments for parameters selection (treated by MIC).	A-15
Figure A-15 Residual stress as a function of depth for Alloy 600 flat plates air laser peened with selected parameters: 10 GW/cm ² irradiance, 18 ns pulse width, 5 layers of peening, and either two layers of tape or polymer spray coating as the ablative layer (treated by MIC).	A-16
Figure A-16 Welded specimen with a one inch by two inches peened surface on side A (top, face of weld) and side B (bottom, weld root). The masked surface is used for the cavitation (water jet) peened specimens only. Dimensions are shown in inches.....	A-17
Figure A-17 Typical side view of the welded plates showing side A (face of weld) and side B (weld root) exposed to the surface	A-17

Figure A-18 Stress measurements with depth for weld specimens were evaluated at 4 locations. The locations in this case (side A) are associated with the weld centerline (locations 1 and 2) and the weld fusion line (locations 3 and 4).....	A-20
Figure A-19 Surface treated specimens with typical stress measurements with depth locations 1, 2, 3, and 4 on side A (left) and side B (right). Locations 2 and 3 are within the peened area and the corresponding locations 1 and 4 are in the untreated area (underwater laser peened specimen shown).....	A-20
Figure A-20 Stress in the longitudinal direction (0°) as a function of distance from the weld center line for untreated welded plates A.....	A-21
Figure A-21 Stress in the transverse direction (90°) as a function of distance from the weld center line for untreated welded plates A.....	A-21
Figure A-22 Stress in the longitudinal direction (0°) as a function of distance from the weld center line for untreated welded plates B.....	A-22
Figure A-23 Stress in the transverse direction (90°) as a function of distance from the weld center line for untreated welded plates B.....	A-23
Figure A-24 Comparison of longitudinal stress (0°) as a function of depth between locations 1, 2, 3, and 4 for untreated welded plate 9A (reference).....	A-23
Figure A-25 Comparison of transverse stress (90°) as a function of depth between locations 1, 2, 3, and 4 for untreated welded plate 9A (reference).....	A-24
Figure A-26 Stress as a function of depth for welded plate specimen 4A underwater laser peened with selected parameters 2.3 GW/cm ² irradiance, 8 ns pulse width, 4500 pulses/cm ² coverage and no ablative layer (treated by Toshiba).....	A-24
Figure A-27 Stress as a function of depth for welded plate specimen 4B underwater laser peened with selected parameters 2.3 GW/cm ² irradiance, 8 ns pulse width, 4500 pulses/cm ² coverage and no ablative layer (treated by Toshiba).....	A-25
Figure A-28 Stress as a function of depth for welded plate specimen 8A underwater laser peened with selected parameters 2.3 GW/cm ² irradiance, 8 ns pulse width, 4500 pulses/cm ² coverage and no ablative layer (treated by Toshiba).....	A-25
Figure A-29 Stress as a function of depth for welded plate specimen 8B underwater laser peened with selected parameters 2.3 GW/cm ² irradiance, 8 ns pulse width, 4500 pulses/cm ² coverage and no ablative layer (treated by Toshiba).....	A-26
Figure A-30 Results of residual stress improvement on the Alloy 600 side of a welded plate	A-26
Figure A-31 Results of residual stress improvement on the Type 304 stainless steel side of a welded plate	A-27
Figure A-32 Test configuration for large diameter applications, provided by Mitsubishi	A-28
Figure A-33 WJP process parameter testing for flat or large radius applications, provided by Mitsubishi	A-28
Figure A-34 Results of residual stress improvement treatment of welded plate at weld location, provided by Mitsubishi	A-30
Figure A-35 Results of residual stress improvement effect of welded plate 25 mm from weld center, provided by Mitsubishi	A-31
Figure A-36 Residual stress profiles before and after WJP in a welded plate with a pre-existing crack, provided by Hitachi-GE	A-32

Figure A-37 Drawing of mock-up fabrication with materials and dimensions indicated (in inches).....	A-33
Figure A-38 Underwater laser peening of BMN-size pipe specimen (left) and BMN mock-up (right) (provided by Toshiba)	A-33
Figure A-39 Treated surfaces (in red) and XRD stress measurement locations (in blue) for underwater laser peened BMN-size pipes (Task 3 specimens) and BMN mock-ups (Task 4 specimens)	A-34
Figure A-40 OD surface residual stress measurement results for pipe specimen No. 1 before surface treatment (as received), after underwater laser peening of OD only, and after underwater laser peening of both OD and ID (treated and measured by Toshiba)	A-35
Figure A-41 OD surface residual stress measurement results for pipe specimen No. 2 before surface treatment (as received), after underwater laser peening of OD only, and after underwater laser peening of both OD and ID (treated and measured by Toshiba)	A-36
Figure A-42 Axial and hoop residual stress with depth measured from the OD of underwater laser peened Alloy 600 BMN-size pipes after OD and ID treatment (by Toshiba)	A-36
Figure A-43 Axial and hoop residual stress with depth measured from the ID of underwater laser peened Alloy 600 BMN-size pipes after OD and ID treatment (by Toshiba)	A-37
Figure A-44 OD surface residual stress measurements results for the pipe and clad section of the mock-up before underwater laser peening (ULP), after ULP on the OD, and after ULP on both the OD and ID (treated and measured by Toshiba).....	A-39
Figure A-45 OD surface residual stress measurements results for the clad section and the weld area of the mock-up before underwater laser peening (ULP), after ULP on the OD, and after ULP on both the OD and ID (treated and measured by Toshiba).....	A-39
Figure A-46 Stress improvement with WJP (Alloy 600—Small Diameter Pipe ID(1/2)), by Hitachi-GE	A-40
Figure A-47 Stress improvement with WJP (Alloy 600—Small Diameter Pipe ID(2/2)), by Hitachi-GE	A-41
Figure A-48 WJP stress improvement effect at a corner location, provided by Hitachi-GE	A-42
Figure A-49 WJP stress improvement effect on pipe inner surface, provided by Hitachi-GE	A-43
Figure A-50 WJP stress improvement effect on pipe outer surface, provided by Hitachi-GE	A-43
Figure A-51 WJP stress improvement effect on a BMN mockup, provided by Hitachi-GE	A-44
Figure A-52 Residual stress values on actual plant component compared with mockup residual stress measurements, provided by Hitachi-GE	A-45
Figure A-53 Mock up Test Block Design, provided by Mitsubishi	A-46
Figure A-54 Locations of Residual Stress Measurements, provided by Mitsubishi	A-47
Figure A-55 Residual Stress at Axial Locations for 0° on 9.5 mm ID Sample – Before WJP, provided by Mitsubishi	A-48

Figure A-56 Residual Stress at Various Depths for 0° Location on 9.5 mm Sample – Before WJP, provided by Mitsubishi	A-48
Figure A-57 Residual Stress at Axial Locations for 0° Location on 9.5 mm Sample – WJP, provided by Mitsubishi	A-50
Figure A-58 Residual Stress at Various Depths for 0° Location on 9.5 mm Sample – WJP, provided by Mitsubishi	A-50
Figure A-59 Results of validation test for cross-section residual stress improvement effect on the BMN inner surface mockup, provided by Mitsubishi.....	A-53
Figure A-60 Visual testing and penetrant testing after WJP on the BMN inner surface mockup, provided by Mitsubishi	A-54
Figure A-61 Location of Microstructure Examinations, provided by Mitsubishi.....	A-54
Figure A-62 Microstructure Examination for ID Configuration Mock-up Test – 9.5 mm ID C-C (100×), provided by Mitsubishi.....	A-55
Figure A-63 Test Coupon Schematic for BMN Verification Testing, provided by Mitsubishi	A-56
Figure A-64 WJP Application using the Tube OD Configuration, provided by Mitsubishi	A-57
Figure A-65 WJP Application using the Large-Radius Surface Configuration, provided by Mitsubishi	A-57
Figure A-66 Location of Residual Stress Measurements, provided by Mitsubishi	A-58
Figure A-67 Residual Stress Results for BMN Mock-Up Test – Tube OD at 0° Location, provided by Mitsubishi.....	A-60
Figure A-68 Residual Stress Results for BMN Mock-Up Test – Tube OD at 180° Location, provided by Mitsubishi	A-61
Figure A-69 Residual Stress Results for BMN Mock-Up Test – Surface of Weld, provided by Mitsubishi	A-62
Figure A-70 Residual Stress Results for BMN Test-Surface of Base-Metal cladding, provided by Mitsubishi.....	A-62
Figure A-71 Visual Inspection Results for BMN Mock-Up Test – 90° Location, provided by Mitsubishi	A-63
Figure A-72 PT Inspection Results for BMN Mock-Up Test – 90° Location, provided by Mitsubishi	A-64
Figure A-73 Microstructure Results for BMN Mock-Up Test – Tube OD 0° Location, provided by Mitsubishi.....	A-64
Figure A-74 Microstructure Results for BMN Mock-Up Test – J-Groove Weld Surface, provided by Mitsubishi.....	A-65
Figure A-75 Microstructure Results for BMN Test – Base-Metal Surface 0° Location, provided by Mitsubishi.....	A-65
Figure A-76 Surface roughness of underwater laser peened surface 20% cold work Type 304 stainless steel – peened with spot diameter of 0.8 mm, pulse energy of 200 mJ, and 3600 pulses/cm ² , provided by Toshiba.....	A-68
Figure A-77 Surface roughness measurement on heat-treated Alloy 600 before and after ULP	A-69
Figure A-78 Surface roughness with 3D measurement method on Type 316L SS after peening, provided by Hitachi-GE	A-69

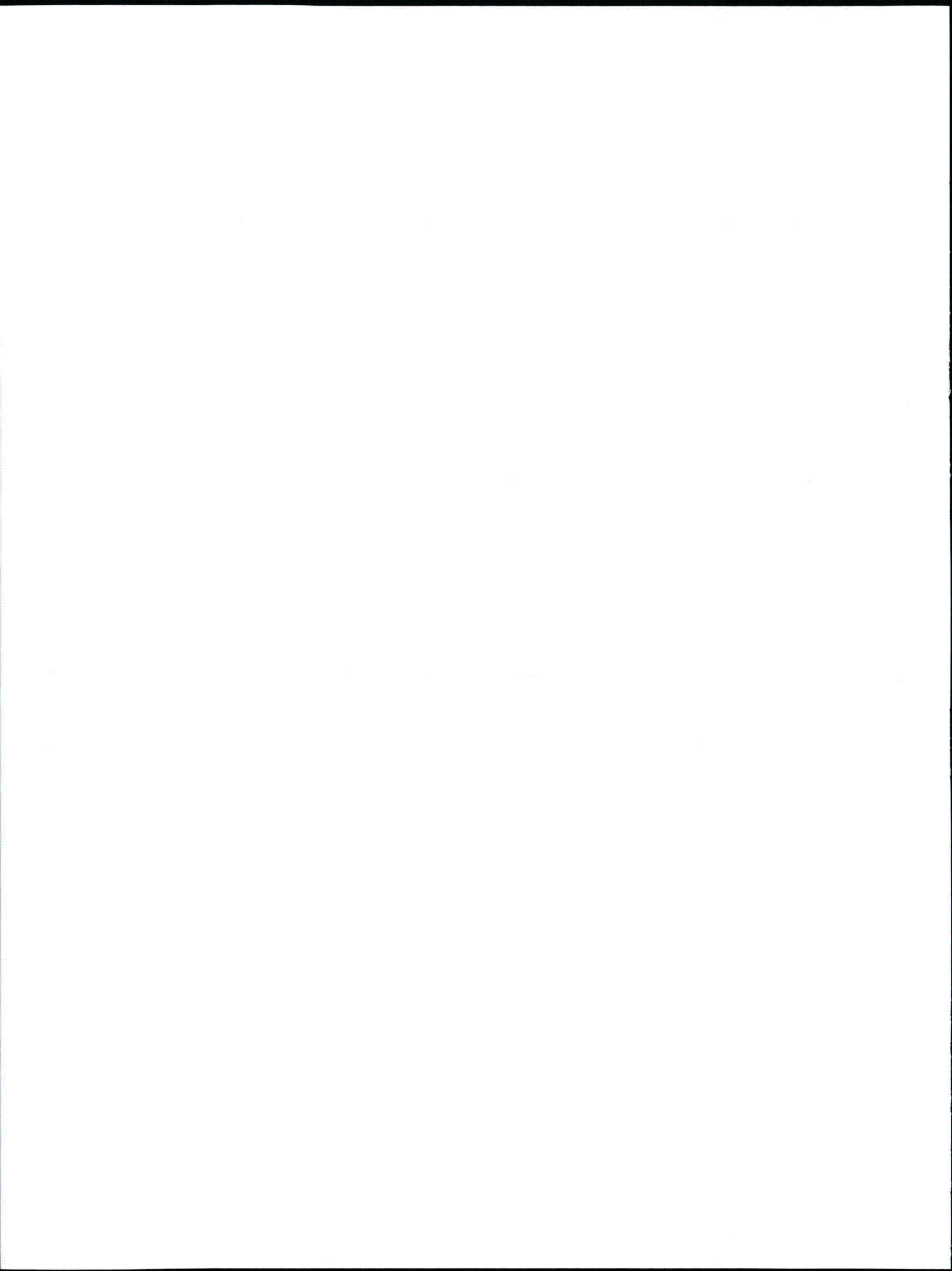
Figure A-79 Surface roughness profile on Type 316L SS after peening, provided by Hitachi-GE	A-70
Figure A-80 Microhardness measurements as a function of depth on the cross section of untreated specimen C-008 (right) and on the cross section of flat plate specimen T-009, underwater laser peened with 2.3 GW/cm ² irradiance, 8 ns pulse width, 4500 pulses/cm ² coverage, and no ablative layer (left) (x100).....	A-71
Figure A-81 Microhardness measurements results for underwater laser peened specimens (treated by Toshiba)	A-71
Figure A-82 Microhardness measurements results for air laser peened specimens (treated by MIC)	A-72
Figure A-83 Hardness depth profile on BMN ID mock-up, 9.5 mm ID tube, at the J-groove weld, 0° orientation, provided by Mitsubishi	A-73
Figure A-84 Hardness depth profiles on BMN OD and J-groove weld mock-up at 45° location (a) tube OD, (b) J-groove weld, and (c) base-metal cladding, provided by Mitsubishi	A-74
Figure A-85 Cross-sectional hardness profile with WJP and SP (Shot Peening), provided by Hitachi-GE	A-76
Figure A-86 Visual Inspection Results for ID Configuration Testing – Stuck Nozzle Test, provided by Mitsubishi.....	A-77
Figure A-87 PT Inspection Results for ID Configuration Testing – Stuck Nozzle Test, provided by Mitsubishi.....	A-77
Figure A-88 Results of (a) Visual Inspections and (b) PT examination for Extreme Conditions on welded flat plate configuration testing, provided by Mitsubishi.....	A-78
Figure A-89 Visual (a) and PT (b) Inspection Results of Tube OD Configuration Verification Test at 0° Location, provided by Mitsubishi.....	A-79
Figure A-90 The CBB test result in 304SS with and without ULP treatment (by Toshiba).....	A-80
Figure A-91 Experiment procedure of PWSCC test on Alloy 132 with and without ULP treatment	A-81
Figure A-92 Summary of PWSCC test.....	A-82
Figure A-93 SCC test of Type 304 stainless steel with and without WJP treatment in boiling 42% MgCl ₂ solution, provided by Hitachi-GE.....	A-83
Figure A-94 CBB test of 304SS with and without WJP treatment to verify the effectiveness of WJP to mitigate SCC susceptibility, provided by Hitachi-GE	A-84
Figure A-95 The schematic of weld and CBB specimen fabrication—The CBB test specimen was 3 mm in thickness and all CBB test coupons were heavily ground	A-85
Figure A-96 Summary of SCC test results—The CBB test exposed Alloy 600/182 weld coupon in pure water with 16 ppm DO at 288°C, with 1% strain to the coupon, provided by Hitachi-GE	A-86
Figure A-97 Visual (upper photograph) and PT (lower photograph) Results for MgCl ₂ Solution Test on an untreated mock-up, provided by Mitsubishi.....	A-87
Figure A-98 Visual (upper photographs) and PT (lower photographs) Results for MgCl ₂ Solution Test Mock-Up treated with WJP, provided by Mitsubishi	A-88
Figure A-99 Partial air laser peening of coupon subsequently loaded by tightening the fixture bolt.....	A-89

Figure A-100 IGSCC crack observed in the unpeened region arrests at the ALP-treated region	A-90
Figure A-101 Test procedure and crack depth distribution for SCC testing of Type 304 stainless steel.....	A-91
Figure A-102 Test procedure and crack depth distribution for SCC testing of Alloy 600	A-92
Figure A-103 Test procedure for testing WJP on existing defects, provided by Mitsubishi	A-93
Figure A-104 Test results of investigation on the effect of WJP application process on existing defects, provided by Mitsubishi.....	A-94
Figure A-105 Toshiba's CBB test for assessing the effectiveness of ULP to a surface with pre-existing defects—The final SCC test was performed in a simulated BWR environment with 8 ppm DO at 288°C for 500 hours. The strain applied in CBB test was 0.5%.....	A-95
Figure A-106 Hitachi-GE investigation of effectiveness of WJP to a surface with pre-existing cracks, provided by Hitachi-GE.....	A-96
Figure A-107 Creviced Bent Beam (CBB) test on pre-cracked sensitized Type 304 stainless steel, provided by Hitachi-GE.....	A-97
Figure A-108 Creviced Bent Beam (CBB) test on the effect of WJP on surface crack propagation, provided by Hitachi-GE	A-98
Figure A-109 Test procedure to investigate the effectiveness of WJP in mitigating further growth of pre-existing SCC cracks, provided by Mitsubishi	A-99
Figure A-110 Residual stress condition after WJP from the peened surface of the BMN size pipe used to assess further SCC growth of pre-existing flaws, provided by Mitsubishi	A-99
Figure A-111 SCC flaw depth following application of WJP and exposure to polythionate solution as a function of initial SCC flaw depth, provided by Mitsubishi.....	A-100
Figure A-112 Plate specimen for determining the effectiveness of inhibiting SCC progress, provided by Mitsubishi.....	A-101
Figure A-113 Weibull plot of latent defect depth (in the case of SUS316) from WJP and USP, provided by Mitsubishi	A-101
Figure A-114 U-Bend specimen.....	A-102
Figure A-115 Cracked U-Bend specimens	A-103
Figure A-116 By application of air laser peening, stress corrosion is arrested in tensioned U-bends of Alloy 600 exposed to corrosive thiosulfate.....	A-103
Figure A-117 As-manufactured Alloy 182 weld deposit on an Alloy 600 plate.....	A-105
Figure A-118 SEM view of cold worked layer induced by “heavy grinding”	A-107
Figure A-119 EBSD analysis of cold worked layer induced by “heavy grinding”	A-108
Figure A-120 Vickers hardness (25 g) profile of “heavily ground” surface.....	A-108
Figure A-121 Loading steps for U-bend specimens (ground face shown in red).....	A-109
Figure A-122 Spring loaded U-bend	A-109
Figure A-123 Comparison of Spring loaded and bolt loaded U-bend specimens.....	A-110
Figure A-124 2-mm-thick and 3-mm-thick spring-loaded U-bends after surface treatments	A-112

Figure A-125 Surface defects observed on U-bend surfaces before exposure to primary water	A-114
Figure A-126 Surface defects observed after pre-ageing period in Primary Water and treatment of U-Bends surface	A-115
Figure A-127 RUB from steam generator (SG) tube WF 422 after 1000 h of exposure to PWR primary water at 360°C	A-120
Figure A-128 U-bends with "heavily ground" surfaces after 1000 h of exposure to PWR primary water at 360°C	A-122
Figure A-129 Stress measurement at the Apex of 3mm thick spring-loaded U-bend	A-125
Figure A-130 Stress measurement at the Apex of 3mm thick bolt-loaded U-bend	A-126
Figure A-131 Stress measurement at the Apex of 2mm thick spring-loaded U-bend	A-127
Figure A-132 Reference system for cracking zones of U-Bend specimens.....	A-128
Figure A-133 RUBs from SG tube WF422 after 1000h and 2000h of exposure to PWR Primary Water at 360°C.	A-129
Figure A-134 UB-GND-2 with "heavily ground" surfaces after 1000 and 3000h exposure to PWR primary water at 360°C.	A-130
Figure A-135 UB-GND-4 with "heavily ground" surfaces after 1000 and 3000h exposure to PWR primary water at 360°C.	A-130
Figure A-136 UB-A4 with "heavily ground" surfaces after 1000 and 3000h exposure to PWR primary water at 360°C.	A-131
Figure A-137 UB-A8 with "heavily ground" surfaces after 1000 h exposure to PWR primary water at 360°C.	A-131
Figure A-138 UB-A2 with "heavily ground" surfaces after 1000 and 3000h exposure to PWR primary water at 360°C.	A-132
Figure A-139 UB-A3 with "heavily ground" surfaces after 1000 h exposure to PWR primary water at 360°C.	A-132
Figure A-140 UB-D3 with "Water Jet Peening" surfaces after 3000 h exposure to PWR primary water at 360°C.	A-133
Figure A-141 UB-D8 with "Water Jet Peening" surfaces after 3000 h exposure to PWR primary water at 360°C.	A-133
Figure A-142 Experimental procedure for investigation of effect of WJP on UT inspectability, provided by Hitachi-GE.....	A-137
Figure A-143 Comparison of measured crack depth before and after WJP in Type 304 stainless steel and Alloy 182, provided by Hitachi-GE	A-138
Figure A-144 Peak vibration frequency as a function of WJP application parameters (stand-off distance and flow rate), provided by Hitachi-GE	A-139
Figure B-1 Procedures for confirmation of residual stress stability on Alloy 600, provided by Toshiba.....	B-2
Figure B-2 Test results on residual stress stability on Alloy 600, provided by Toshiba	B-2
Figure B-3 Thermal Stress Relaxation test on Alloy 600 at 350°C for 1646 h	B-3
Figure B-4 Shakedown test (strain cycles (tensile)), Type 304 SS/Alloy 182/Alloy 600), provided by Hitachi-GE	B-4
Figure B-5 Specimen for Cyclic Stress Relaxation Testing, provided by Mitsubishi	B-5

Figure B-6 Results of Cyclic Stress Relaxation Testing, provided by Mitsubishi	B-6
Figure B-7 Test Procedure for High Temperature Load Cycling Experiments by Mitsubishi	B-7
Figure B-8 Results of High Temperature Load cycling experiments by Mitsubishi	B-7
Figure B-9 Thermal relaxation test (Alloy 600 / Alloy 182 / 316L SS) at 450°C, provided by Hitachi-GE	B-9
Figure B-10 Specimen for Relaxation Testing Under High Temperature Environment, provided by Mitsubishi	B-10
Figure B-11 Results of High Temperature Relaxation Testing, provided by Mitsubishi	B-12
Figure B-12 Schematic drawing of the autoclave loop IK-610	B-14
Figure B-13 General view of the autoclave internals and part of the chain with interconnected samples	B-15
Figure B-14 Microstructure of the sample material	B-16
Figure B-15 Drawing of the test sample with dimensions in mm (sample thickness is 12.5 mm)	B-17
Figure B-16 Comparison of the Microstructure of the Material Available for this Project (left) and the Material Used for the First Set of Experiments (right)	B-19
Figure B-17 All samples prepared for exposure	B-21
Figure B-18 Appearance of the as-manufactured samples after different stages of the experiment	B-21
Figure B-19 Subsurface layer microstructure of the as-manufactured sample	B-22
Figure B-20 Microhardness depth profile of the as-manufactured sample	B-23
Figure B-21 Surface stresses measured parallel (left) and perpendicular (right) to the loading direction, as-manufactured	B-23
Figure B-22 All samples prepared for exposure after underwater laser peening by Toshiba	B-24
Figure B-23 Appearance of the samples after different stages of experiment: ULP by Toshiba	B-25
Figure B-24 Subsurface layer microstructure: ULP by Toshiba	B-26
Figure B-25 Microhardness depth profile: ULP by Toshiba	B-27
Figure B-26 Surface stresses measured parallel (left) and perpendicular (right) to the loading direction: ULP by Toshiba	B-28
Figure B-27 All samples prepared for exposure after water jet peening by Hitachi-GE	B-29
Figure B-28 Appearance of the samples after different stages of experiment: WJP by Hitachi-GE	B-30
Figure B-29 Subsurface layer microstructure: WJP by Hitachi-GE	B-31
Figure B-30 Microhardness depth profile: WJP by Hitachi-GE	B-31
Figure B-31 Surface stresses measured parallel (left) and perpendicular (right) to the loading direction: WJP by Hitachi-GE	B-32
Figure B-32 Samples prepared for exposure after water jet peening, Mitsubishi	B-33
Figure B-33 Appearance of the samples after different stages of the experiment: WJP by Mitsubishi	B-34

Figure B-34 Subsurface layer microstructure: WJP by Mitsubishi	B-35
Figure B-35 Microhardness depth profile: WJP by Mitsubishi	B-36
Figure B-36 Surface stresses measured parallel (left) and perpendicular (right) to the loading direction: WJP by Mitsubishi.....	B-36
Figure B-37 Appearance of the samples after different stages of experiment: ALP by MIC.....	B-37
Figure B-38 Microstructure of the sample after peening and before exposure (micrographs on left) and close-up of the surface (right)	B-38
Figure B-39 Microstructure of the sample after exposure (8 cycles), upper and lower surface, different magnifications: ALP by MIC	B-39
Figure B-40 Microhardness depth profile: ALP by MIC.....	B-40
Figure B-41 Comparison of MHV Indent Sizes in Large and Small Grain Areas.....	B-41
Figure B-42 Surface stresses measured parallel (left) and perpendicular (right) to the loading direction: ALP by MIC	B-42
Figure B-43 Comparison of MHV Depth Profile Results in both sets of experiments	B-44



LIST OF TABLES

Table 3-1 Experience of WJP and ULP for Japanese PWR plants	3-6
Table 3-2 Experience of WJP and ULP for Japanese BWR plants	3-7
Table 3-3 ULP on PWRs performed in Japan.....	3-8
Table 3-4 Japanese experience using WJP on PWRs	3-8
Table 4-1 Summary of Activation Energy Values for Alloy 600 Stress Relaxation	4-11
Table 4-2 Lifetime Equivalency of Hot Leg Butt Welds Operating at 329°C	4-12
Table 4-3 Lifetime Equivalency of CRDMs Operating at 315°C	4-13
Table 4-4 Relationship between Cold Reduction, Hardness and Tensile Strength for Alloy 600	4-17
Table 4-5 Effects of Hitachi-GE Water Jet Peening and Standard Shot Peening on Hardness and Percent Cold Work of Alloy 600 and Alloy 182	4-18
Table 4-6 Effects of MHI Water Jet Peening on Hardness and Percent Cold Work of Alloy 600 and Alloy 132.....	4-19
Table 4-7 Effects of Westinghouse – Toshiba Underwater Laser Peening on Hardness and Percent Cold Work of Alloy 600	4-19
Table 5-1 ULP control parameters	5-2
Table A-1 Test Data at two different locations on an unpeened welded plate, provided by Mitsubishi	A-29
Table A-2 Test Data at two different locations on a peened welded plate, provided by Mitsubishi	A-30
Table A-3 Residual Stress Measurements from Validation Test for ID Configuration – 9.5 mm ID before WJP, provided by Mitsubishi	A-47
Table A-4 Data from Validation Test for ID Configuration – 9.5 mm ID, provided by Mitsubishi	A-49
Table A-5 Data from Validation Test for ID Configuration – 16.0 mm before WJP, provided by Mitsubishi.....	A-51
Table A-6 Data from Validation Test for ID Configuration – 16.0 mm ID, provided by Mitsubishi	A-52
Table A-7 Residual Stresses for BMN Verification Testing – OD Tube Surface, provided by Mitsubishi	A-59
Table A-8 Residual Stresses for BMN Verification Testing – Large Radius Surfaces, provided by Mitsubishi.....	A-60
Table A-9 Surface roughness of evaluated peening processes on Alloy 600 flat plates	A-67
Table A-10 Chemical analysis of Soudonel CQ5 welding rods used to manufacture the Alloy 182 weld deposit	A-106

Table A-11 Grinding parameters for transverse laboratory heavy grinding	A-107
Table A-12 Distance between legs of spring-loaded U-bend after surface treatments	A-112
Table A-13 Displacement of legs of spring-loaded U-Bend specimens after mechanical surface mitigation treatments.	A-113
Table A-14 Complete test matrix for “mechanical” remedial methods	A-116
Table A-15 Complete test matrix for “mechanical” remedial methods	A-117
Table A-16 XRD measurements of surface stress and cold work on U-bends before and after “mechanical” surface mitigation treatments	A-119
Table A-17 Results of 1000 h exposure test on Alloy 182 and Alloy 600 U-bends	A-121
Table A-18 XRD measurements of surface stresses on U-Bends before and after corrosion test	A-123
Table A-19 Results of 1000+2000 h of exposure on Alloy 182 U-bends / new mechanical mitigation methods.	A-134
Table A-20 Results of 1000+2000 h of exposure on Alloy 182 U-bends / new mechanical mitigation methods.	A-135
Table B-1 Data for Temperature Relaxation Testing, provided by Mitsubishi	B-11
Table B-2 Chemical analysis of the primary medium	B-15
Table B-3 Alloy 600 chemical composition and mechanical properties provided in the certificate	B-17
Table B-4 Vendors, peening processes, and samples used for first set of tests	B-18
Table B-5 Stress relaxation test matrix	B-20
Table B-6 Sample Numbering for ALP treated specimens	B-20
Table B-7 Results of the stress measurements: as-manufactured	B-24
Table B-8 Results of the stress measurements: ULP, Toshiba	B-29
Table B-9 Results of the stress measurements: WJP, Hitachi-GE	B-33
Table B-10 Results of the stress measurements: WJP, Mitsubishi	B-37
Table B-11 Results of the stress measurements: ALP, MIC	B-42
Table B-12 Comparison of Average Values of the Surface Stresses from the First and Second Set of Experiments	B-43

1

INTRODUCTION

1.1 Background

1.1.1 *Need Addressed by Surface Stress Improvement (SSI) Techniques*

During the past two decades, stress corrosion cracking (SCC) has become the most relevant phenomenon affecting nuclear plant availability and plant lifetime management. SCC can lead to increased costs for operation, maintenance, assessment, repair, and replacement of boiling water reactor (BWR) and pressurized water reactor (PWR) components.

Alloy 600 and 82/182 materials, which are widely used in PWR systems, are susceptible to primary water stress corrosion cracking (PWSCC). PWSCC has been reported in U.S. and international plants on reactor pressure vessel top head penetration nozzles (RPVHPNs), reactor vessel bottom mounted nozzles (BMNs), and dissimilar metal welds (DMWs) of primary system piping, as well as on other Alloy 600/82/182 pressure boundary components such as steam generator tubes and plugs, pressurizer heater sleeves, pressurizer instrumentation nozzles, and reactor hot-leg piping instrumentation nozzles (see for example, [1], [2], [3], [4], [5], [6], [7], [8], [9]). To ensure the integrity of PWR primary systems, Materials Reliability Program (MRP) guidelines and ASME (the American Society of Mechanical Engineers) Code cases have been developed to specify augmented inspection requirements for Alloy 600/82/182 pressure boundary components. Inspection requirements and their technical bases are provided for RPVHPNs in ASME Code Case N-729-1 [10] and MRP-117 [11], for BMNs in ASME Code Case N-722-1 [1] and MRP-206 [12], and for DMWs in primary system piping in ASME Code Case N-770-1 [13] and MRP-139, Revision 1 [14]. In addition, SCC is a key degradation mechanism for reactor internals, and relevant examination requirements are well defined in MRP-227 [15] and MRP-228 [16].

It is widely recognized that SCC, including PWSCC, is caused by a combination of three factors—tensile surface stress, susceptible material, and the elevated temperature environment of PWR coolant. Therefore, SCC can be mitigated by removing one or more of those three factors. This has led to application of various mitigation techniques at U.S. PWRs, including shot peening, mechanical stress improvement, weld overlay, and coolant chemical control, as well as component replacements using SCC-resistant materials. However, some Alloy 600/82/182 components cannot be mitigated by the current methods or economically replaced. Such components include RPVHPNs (control rod drive mechanism (CRDM), control element drive mechanism (CEDM), top head instrumentation, and head vent nozzles), BMNs, and some piping DMWs, in particular those with limited access at the pipe exterior. For these components, viable solutions are still needed in order to mitigate PWSCC, avoid costly replacements, and reduce the inspection burden.

Other potential solutions that are amenable to application for these component locations include laser peening, water jet (i.e., cavitation) peening, weld in-lay, weld on-lay, electropolishing, surface renewal, and ultrasonic shot peening. These are surface processes that eliminate either the tensile stress of the susceptible material in contact with the primary coolant, or cover the component inside surface with a layer of PWSCC-resistant material.

This Materials Reliability Program (MRP) report focuses on the surface stress improvement (SSI) techniques of laser peening (LP) and water jet peening (WJP). These methods operate by impact of a pressure shock wave, which introduces a compressive residual stress on the treated surface. The shock wave may be produced via laser energy (laser peening, LP) or via a water jet impinging on the surface (water jet peening, WJP). Although the two LP processes covered by this report operate by the same physical principles, they are discussed separately because of the significant differences in process parameters and equipment, specifically differences in laser spot size, laser pulse energy level, and beam delivery equipment. For the purpose of this report, the LP process developed by Toshiba/Westinghouse is termed underwater laser peening (ULP) as it historically has been performed in an underwater environment, and the LP process developed by Metal Improvement Company (MIC) is termed air laser peening (ALP) as it historically has been applied in an air environment. However, there is flexibility in the LP techniques such that each could be adapted to both types of environments.

1.1.2 Commercialization of Underwater Laser Peening (ULP) and Water Jet Peening (WJP) Processes

As described in detail in Section 2, the ULP and WJP methods have historically been performed underwater. In each method, a shock pressure is produced at the treated surface resulting in a layer of compressive residual stress to a depth of roughly 1 millimeter (0.04 in.). As described below, the ULP and WJP methods have been widely applied at Japanese BWR and PWR plants. Considering this extensive operating experience with SSI treatments in Japanese LWR plants, no corrosion cracking has been observed during in-service inspection (ISI) since the treatments began, which supports both their effectiveness at achieving the expected compressive surface status and their sustainability during plant operation. The accrued operating experience and particular system designs benchmarked through mockup testing and field application have generated a convenient platform for applying ULP and WJP at U.S. and international nuclear plants. Thus, ULP and WJP are PWSCC mitigation methods that have been commercialized for use in PWRs.

1.1.3 Use of Underwater Laser Peening (ULP) and Water Jet Peening (WJP) in Japanese BWRs and PWRs

As an important part of mitigation efforts, the SSI techniques of ULP¹ and WJP have been applied at many Japanese BWRs and PWRs over the past 13 years. SSI mitigation in Japan has

¹ The process used by Toshiba for laser peening in its initial applications in Japan involved the use of fiber optical cables, and was called fiber laser peening. Starting in about 1998 Toshiba introduced a portable laser system that, in some applications, does not include any fiber optics, i.e., it uses other optical transmission methods. At about this time, Toshiba changed the name used for its process to "laser peening" from "fiber laser peening." The term "underwater laser peening (ULP)" is used specifically in this report for laser peening by Toshiba whether or not the process involved use of fiber optical cables.

covered austenitic stainless steel components and nickel-based alloy components in BWRs such as core shroud and CRD stub tube and reactor internals and nickel-alloy components in PWRs such as BMNs (including the J-groove attachment weld) and RV outlet/inlet nozzle DMWs. As of summer 2012, 23 out of 24 PWR units in Japan have applied ULP or WJP to the BMNs including the J-groove attachment welds (Table 3-1). The remaining unit in the PWR fleet plans to apply peening treatment to BMNs including the J-groove welds in the coming years. With regard to the BWRs, as of 2012, the core shrouds or bottom head penetrations at 20 BWR units have been treated with either WJP or ULP, and WJP has also been applied to three advanced boiling water reactor (ABWR) units during the fabrication or construction phase (Table 3-2). In addition, Hitachi-GE had plans to apply WJP to additional BWR units during their outages and new ABWR units.

1.1.4 Commercialization of Air Laser Peening (ALP) Process

In the ALP method, a shock wave is created that penetrates into the metal and plastically compresses the surface layer creating a compressive residual stress to a depth of 1-8 mm depending on the material, component geometry, and laser peening parameters. Although ALP has not yet been performed in nuclear power plants, it is actively applied as a commercialized technology in critical aerospace applications. As described in this report, ALP technology is readily adaptable to PWR applications, and an extensive base of experience is available supporting its effectiveness.

Air laser peening has emerged as a leading technology that extends the fatigue life and improves fatigue strength of a wide variety of metal alloys in a broad range of applications and industries. The technology is currently being utilized extensively by the commercial aerospace industry to prevent the fretting fatigue of highly stressed rotating turbine engine components and more recently by the U.S. military for extending the lifetime of important assets such as F-22 fighter jets. ALP is being widely used in the commercial sector for advanced generation aircraft such as the 777, 747-8, 787, and Gulfstream V and VI. Commercially it has Federal Aviation Administration (FAA) and European Aviation Safety Agency (EASA) acceptance in flight turbines and recently for the first time from the design stage in structures on the 747-8 application.

ALP has been shown to be effective at mitigating SCC and fatigue, and there is also potential value in impeding the degradation process of hydrogen embrittlement. ALP is amenable to application to critical nuclear power plant components such as welded subassemblies, fittings, pipes, flanges, and vessel penetrations. Over the past decade, there have been key advances in ALP technology including higher speed processing, transportable technology that operates in the field, and precision robotic beam delivery with remote control processing. As it is applied under full computer control, it is considered to be a reliable, highly predictable, and repeatable technology.

1.2 Purpose

The purpose of this report is to establish the technical basis for applying surface stress improvement (SSI) treatments in mitigating PWSCC as a viable method to protect key PWR plant assets. The research targets the following specific goals:

- To establish a technical basis supporting the application of SSI treatments that can be routinely applied in PWR plants, as needed by plant owners throughout the industry
- To establish the effectiveness of SSI treatments (especially laser and water jet peening) as alternative mitigation options to be applied in the nuclear industry
- To present information on implementation of these SSI treatments that EPRI members can consider in pursuing proactive mitigation options
- To identify Alloy 600/82/182 locations for which relaxation of inspection requirements is appropriate after applying SSI mitigation treatments

1.3 Scope

This study addresses ULP, ALP, and WJP as SSI mitigation techniques for Alloy 600/82/182 locations in PWRs. The focus of the report is on RPVHPNs (i.e., CRDM/CEDM nozzles and other nozzles installed with J-groove attachment welds such as top head instrumentation nozzles and head vent nozzles), BMNs (i.e., bottom mounted instrumentation (BMI) nozzles, in-core instrumentation (ICI) nozzles, and incore monitoring instrumentation (IMI) nozzles), and DMWs in the primary piping system. In each case, the SSI treatment is applied to the entire area of the wetted surface that is susceptible to PWSCC. In the case of RPVHPNs and BMNs, the susceptible area is comprised of the wetted surface of the high stress region at the ID of the Alloy 600 nozzle tube near its attachment to the head inside surface, along with the wetted surface of the Alloy 82/182 J-groove attachment weld including the wetted surface of the adjacent Alloy 82/182 weld butter and Alloy 600 base material. In the case of piping DMWs, the susceptible area is comprised of the entire wetted surface of the Alloy 82/182 weld material in contact with the primary coolant.

1.4 Approach

This report provides a comparative summary of current SSI techniques that may be used to mitigate PWSCC in PWRs. Operating principles, system design, and field implementation issues are presented for the ULP, ALP, and WJP techniques. In addition, the results of extensive experimental studies—among them corrosion cracking and stress relaxation tests—are presented supporting the long-term effectiveness of these mitigation methods without any unacceptable side effects. These experimental studies include independent tests sponsored by EPRI, as well as tests by SSI vendors. The MRP plans additional work to support the use of SSI techniques in PWRs, including development of relaxed intervals for periodic inspections based on the information presented in this report.

The intent is to provide the technical justification for alternative mitigation options for utilities addressing PWSCC concerns for RPVHPNs, BMN, and DMW locations such as RV inlet/outlet nozzle welds.

1.5 Report Organization

The organization of this report is described below.

1. INTRODUCTION (SECTION 1)

This introductory section provides a brief background discussion, defines the purpose and scope of this study, and describes the approach used. Section 1 also presents the extensive experience with ULP and WJP at Japanese BWRs and PWRs, demonstrating that peening is a technically viable solution.

2. THEORY AND TECHNOLOGY OF SURFACE STRESS IMPROVEMENT (SECTION 2)

Section 2 presents detailed background information on the operating principles and commercialized technology for the ULP, ALP, and WJP techniques.

3. RELEVANT PLANT PEENING EXPERIENCE (SECTION 3)

Section 3 describes relevant plant experience related to peening used as a mitigation measure against PWSCC in PWRs and SCC in BWRs. Experience in both PWRs and BWRs is described, as is use of peening in PWR steam generators and for Alloy 718 bolting used in PWR fuel assembly applications.

4. EFFECTIVENESS OF SURFACE STRESS IMPROVEMENT (SECTION 4)

In the context of the key criteria for demonstrating the long-term effectiveness of SSI methods for mitigating PWSCC, Section 4 summarizes the extensive test data presented in Appendices A and B. These data include stress measurements, corrosion cracking testing, stress relaxation tests, and load cycling tests, as well as other types of tests supporting the effectiveness of the SSI methods and lack of unacceptable side effects.

5. IMPLEMENTATION CONSIDERATIONS OF LASER AND WATER JET PEENING TECHNIQUES (SECTION 5)

Section 5 summarizes the key practical implementation issues associated with the ULP, ALP, and WJP techniques. Unlike the ALP technique, the ULP and WJP techniques have historically been performed underwater. All three techniques are applicable to treatment of RPVHPNs, BMNs, and piping DMWs. Specialized tooling would be necessary to apply WJP to the outer diameter surface and J-groove weld of RPVHPNs including CRDM/CEDM nozzles given that mitigation would be performed while the head is located on its storage stand. In the case of ULP, demonstration work including mockup testing and field experience has been performed in an underwater environment, but the process can be adapted to be performed in air. Use of ALP for BMN or piping DMW locations would require that these areas be drained during the maintenance outage, or that the laser beam be piped to the underwater target location.

6. CONCLUSIONS AND RECOMMENDATIONS (SECTION 6)

Section 6 presents key conclusions and recommendations regarding SSI as a method to mitigate PWSCC of Alloy 600/82/182 components in PWRs.

7. REFERENCES (SECTION 7)

Section 7 lists the references cited in this report including the two appendices.

8. APPENDIX A: EXPERIMENTAL VERIFICATION OF EFFECTIVENESS OF SURFACE STRESS IMPROVEMENT TO MITIGATE PWSCC

Appendix A presents various experimental studies supporting the effectiveness of the ULP, ALP, and WJP techniques. These studies include stress measurements and corrosion testing of the treated surface. Some tests were performed using simplified test sample configurations such as flat plates and U-bend samples, and others used mockup test samples to confirm the effectiveness of the process for actual plant geometries of interest. The experimental studies include independent tests sponsored by EPRI, as well as tests by SSI vendors.

9. APPENDIX B: LONG-TERM EFFECTIVENESS OF SURFACE STRESS IMPROVEMENT

Appendix B presents additional experimental studies that address the long-term effectiveness of the laser and water jet peening methods under PWR conditions. These experimental studies investigate the effect of relaxation of the peening compressive residual stress due to exposure to plant operating temperature, as well as stress shakedown effects due to load cycling. Again, the experimental studies include independent tests sponsored by EPRI, as well as tests by SSI vendors.

2

THEORY AND TECHNOLOGY OF SURFACE STRESS IMPROVEMENT

2.1 Introduction

It is well recognized that PWSCC susceptibility is strongly dependent on a combination of three factors: tensile surface stress, susceptible material, and the elevated temperature environment of PWR coolant. Therefore, PWSCC can be mitigated by removing one or more of those three factors (see Figure 2-1). This has led to the development of various mitigation techniques including surface stress improvement (SSI), weld overlay, weld in-lay, weld on-lay, mechanical stress improvement, and coolant chemical control.

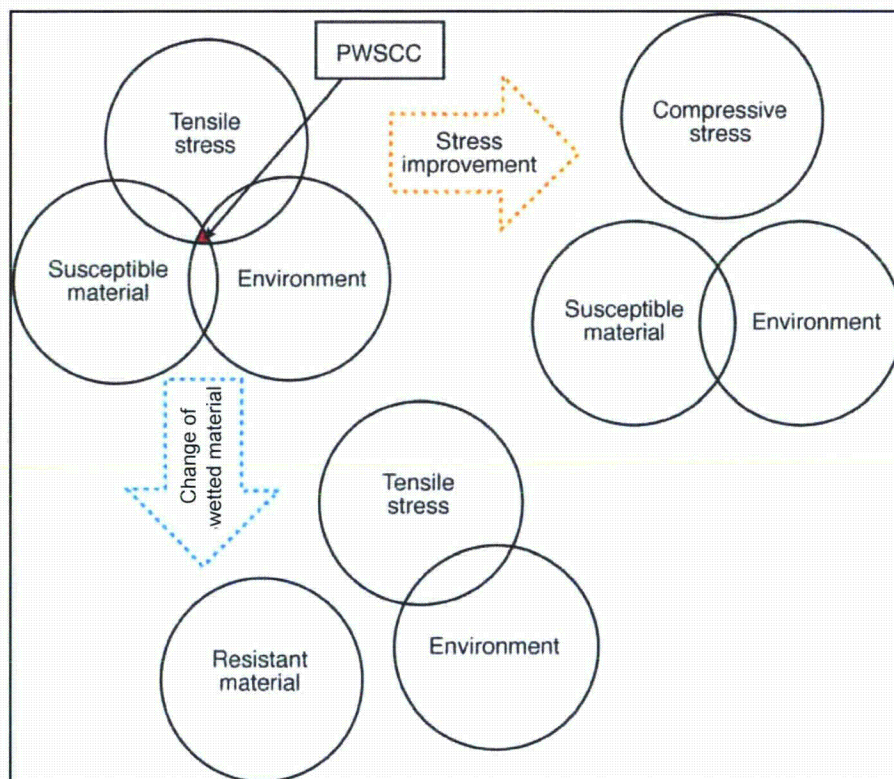


Figure 2-1
PWSCC mitigation by surface treatment

Among those mitigation processes, SSI treatment creates compressive stress at the surface of treated components. Common SSI techniques applicable to LWR components include water jet peening (WJP), laser peening (LP), surface renewal, electropolishing, and shot peening

(including ultrasonic shot peening (USP)). In comparison, the weld in-lay and weld on-lay techniques introduce a layer of PWSCC-resistant material between the susceptible material and the PWR coolant.² In addition, surface composition changes can also be realized through a chemical process such as electropolishing or the EPRI-patented chrome deposition process (chromization) [18]. Of all these surface treatments, WJP and ULP are distinct from the others in that they have historically been performed underwater. The underwater processes may be advantageous if the area to be treated is usually flooded during refueling outages, while specialized tooling may be necessary to apply WJP to a component that is not normally flooded during refueling outages. In the case of ULP, demonstration work including mockup testing and field experience has been performed in an underwater environment, but the process can be adapted to be performed in air. SSI could be applied after weld in-lay or weld on-lay to further improve the resistance to PWSCC of the new material in contact with the reactor coolant. Different from surface treatment, weld overlay [2] is another important repair and mitigation technique widely used in BWR and PWR piping weld repair. Weld overlays provide additional structural reinforcement (with SCC-resistant material) and provide a favorable residual stress reversal to stop the growth of existing cracks. USP has been used in Japan in locations where application is done without a wetted surface, and it represents another alternative for PWSCC mitigation.

Although each technique has its own specific advantages, this document focuses on the surface stress improvement techniques of underwater laser peening (ULP), water jet (i.e., cavitation) peening (WJP), and air laser peening (ALP). For other mitigation measures such as weld overlay and weld on-lay/in-lay methods, details can be found in related MRP documents [2], which include implementation guidance. Information on ultrasonic shot peening, which has been widely used as a PWSCC mitigation measure in Japan, can be found in vendor prepared technical literature [19].

Section 2.2 below addresses ULP, Section 2.3 addresses WJP, and Section 2.4 addresses ALP. Section 2.5 presents key conclusions. Note that the material in Section 2 includes basic information on the effect of these SSI techniques on the stress profile at the treated surface. Section A.1 of Appendix A compiles additional experimentally measured stress profiles, focusing on data for Alloy 600/82/182 samples and mockups of PWR plant components.

2.2 Underwater Laser Peening (ULP)

2.2.1 ULP Surface Treatment Technologies and Principles of Operation

The physical principle involved in laser peening treatment is considered to be an energy conversion procedure from laser to shock wave that results in material plastic deformation. When a nanosecond-order laser pulse focuses on a water-immersed metal material, the top surface absorbs the laser energy and evaporates instantaneously through ablative interaction, as shown in Figure 2-2. The evaporating metal material is confined since the inertia of surrounding water inhibits the expansion of the metal vapor. The resulting high-density metal vapor is immediately

² ASME Code Case N-766 [17] defines weld in-lay as “a corrosion resistant barrier applied on the inside surface of the component between the stress-corrosion-cracking (SCC) susceptible material and the reactor coolant, requiring excavation of some portion of the SCC susceptible material.” N-766 defines weld on-lay in the same manner, except that excavation of SCC susceptible material is not required.

ionized to form plasma by inverse Bremsstrahlung, the absorption of high-intensity radiation by electrons in the field of nuclei. Subsequent laser energy absorption in the plasma generates a heat-sustained shock wave, which impinges on the surface of the metal material with an intensity of several GPa, far exceeding the yield strength of the metal. The shock wave propagates into the metal interior and loses energy as it creates a permanent strain on the metal material. After the passage of the shock wave, the permanent strain remains and the surrounding metal material constrains the strained region as a reaction to elastic strain, thus forming a compressive residual stress on the metal surface.

The process capability is equal to the pulse repetition rate (Hz) divided by the irradiating pulse density (pulses per unit area). Thus, it largely depends on the actual system used for peening. For instance, if a laser system with 300 Hz is used and the material is peened with a pulse density of 1800 pulses/cm², then the processing speed is 10 cm²/min. and if 120 Hz and 4500 pulses/cm² are used, then it is 1.6 cm²/min.

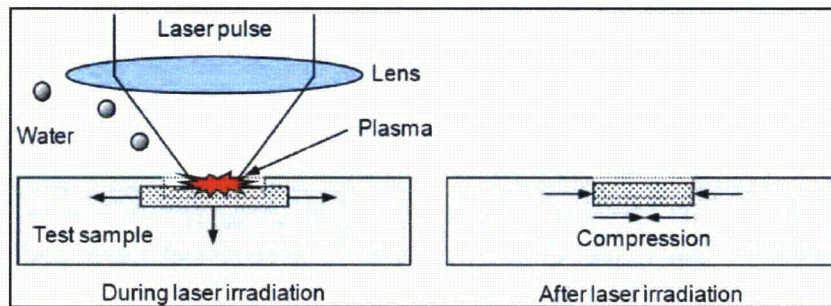


Figure 2-2
Fundamental process of laser peening treatment, by Toshiba

2.2.2 Numerical Analysis and Experimental Verification of ULP

Laser peening treatment changes the stress field in a metal material from tensile to compressive by the impulsive pressure developed by a laser-induced plasma. As shown in Figure 2-3, the plasma, in this example generated by the irradiation of a frequency-doubled Nd:YAG laser on Type 304 stainless steel, has been directly observed by imaging the plasma luminescence. By comparing the observed image to calculations, the time evolution was calibrated for the calculated plasma pressure. The propagation of a shock wave induced by laser irradiation and the dynamic response of the material were simulated by elasto-plastic analysis with a finite element program, using the plasma pressure as an external load. The calculated residual stress was then compared to the result of the corresponding experiment as shown in the following sections.

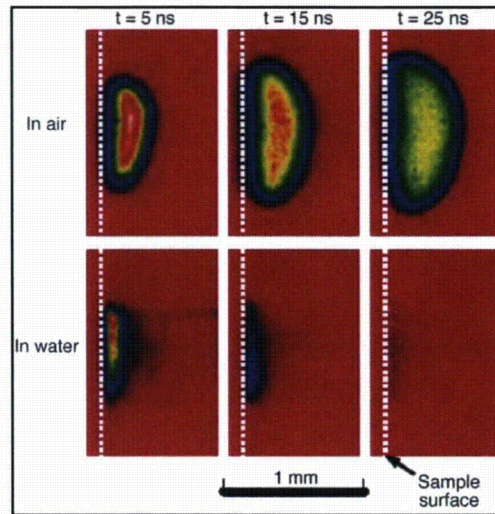


Figure 2-3
Plasma generated by laser irradiation in air and in water, by Toshiba

2.2.2.1 Laser-Induced Plasma Pressure

In the framework of the one-dimensional hydrodynamic model shown in Figure 2-4, the plasma pressure P , the thickness L , and the expansion velocity V during laser irradiation are calculated as functions of time t with the following equations:

$$I(t) = P(t) \frac{dL(t)}{dt} + \frac{3}{2\alpha} \frac{d[P(t)L(t)]}{dt} \quad [2-1]$$

$$V(t) = \frac{dL(t)}{dt} = \left[\frac{1}{Z_1} + \frac{1}{Z_2} \right] P(t) \quad [2-2]$$

where I is the laser intensity. The shock wave impedance Z_i is defined as $Z_i = \rho_i D_i$, where ρ_i and D_i are the density and the shock velocity, respectively. The index i represents the laser irradiated material ($i = 1$) or water ($i = 2$). The plasma is considered to be a perfect gas here. The corrective factor α corresponds to the ratio of thermal to plasma internal energy (for a perfect gas, $\alpha = 1$).

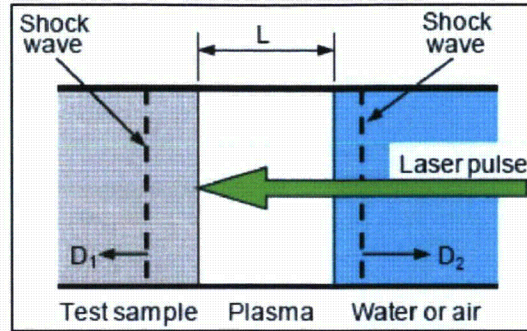


Figure 2-4
One-dimensional model of laser-induced plasma, by Toshiba

Assuming adiabatic cooling of the plasma, P , L , and V can be obtained after laser irradiation by solving the following equation coupled with Equation [2-2]:

$$P(t) = P(\tau) \left[\frac{L(\tau)}{L(t)} \right]^\gamma \quad [2-3]$$

where τ is the laser switched-off time and γ is the specific-heat ratio. In the case of laser irradiation in air, the shock impedance Z_2 in Equation [2-2] should be written as:

$$Z_2 = \left(\frac{\gamma + 1}{2} \rho_2 P \right)^{\frac{1}{2}} \quad [2-4]$$

instead of $Z_2 = \rho_2 D_2$.

The parameter α in the analytical model was estimated to be 0.2 to reproduce the observed results in corresponding experiments. The time evolution of the plasma pressure in the laser peening treatment can be calculated using the above equations.

2.2.2.2 Material Properties and Calculation System for Theoretical Analysis

Figure 2-5 shows the stress-strain relations obtained from static tensile tests for the as-received (without cold working) and 20% cold-worked Type 304 stainless steel used in this theoretical analysis. Young's modulus (E) and yield strength (σ_y) of the as-received material are 1.48×10^5 MPa and 234 MPa, respectively, whereas they are 1.10×10^5 MPa and 658 MPa for the 20% cold-worked material. Poisson's ratio is assumed to be 0.28 for both materials.

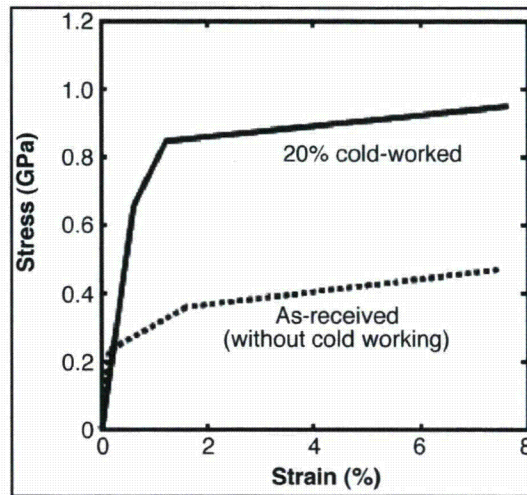


Figure 2-5
Stress-strain relations of Type 304 stainless steel, by Toshiba

A finite element model to analyze the laser peening treatment is shown in Figure 2-6. The center of the laser irradiated spot was set to the origin of the (r, θ, z) coordinate system.

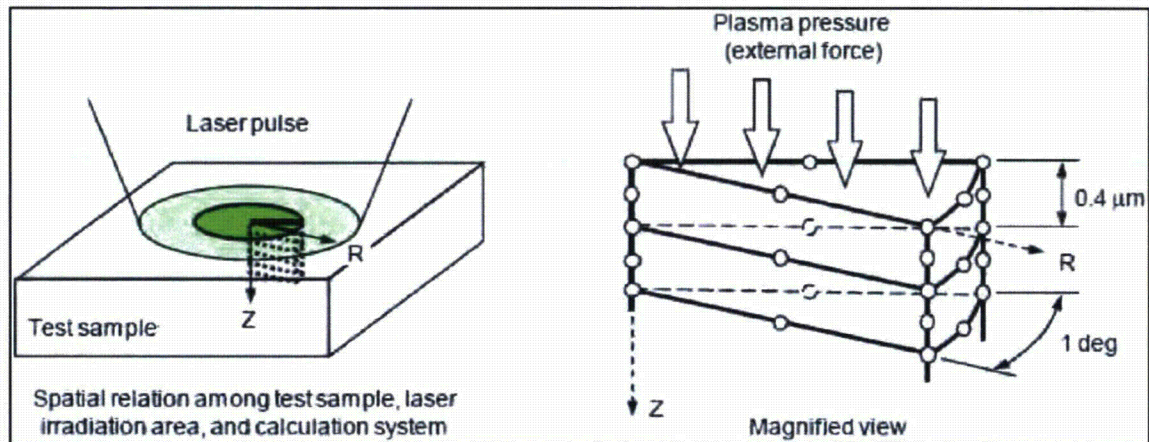


Figure 2-6
Finite element model for calculation of shock wave propagation, by Toshiba

Considering the axial symmetry of the problem, the cylindrical calculation system can be reduced to a wedge with a central angle of one degree. The wedge was discretized into 5000 sectors stacked in the z -direction using a 20-node isoparametric solid element. The degree of freedom (DOF) is constrained in the r - and θ -directions for all the nodes in the calculation system, which means the shock wave propagates in the z -direction as a plane wave without stretching of the wave front. The total thickness of the calculation system is 2 mm, and the thickness of each element is $0.4 \mu\text{m}$, which is one order of magnitude smaller than the propagation length of the shock wave in 1 ns. The time evolution of the stress along the z -axis

was calculated to show the propagation of the shock wave and the resulting residual stress profile.

2.2.2.3 Experimental Verification

To calibrate the theoretical model above, experimental tests were performed, as described in this section. A schematic of the experimental setup on the laser peening treatment is shown in Figure 2-7. The fundamental wave of a compact and commercially available Q-switched Nd:YAG laser ($\lambda = 1.06 \mu\text{m}$) is frequency-doubled to a water-penetrable wave ($\lambda = 532 \text{ nm}$) by a second harmonic generator (SHG) with a nonlinear optical crystal. The laser pulse energy incident on a test sample is adjusted with a variable attenuator and monitored with an energy meter. The pulse duration is about 8 ns in FWHM (full width at half maximum), and the temporal profile is monitored with a photodiode. The test sample is fixed on a sample holder and driven to x- and y-directions in a water jacket during laser irradiation, as shown in Figure 2-8.

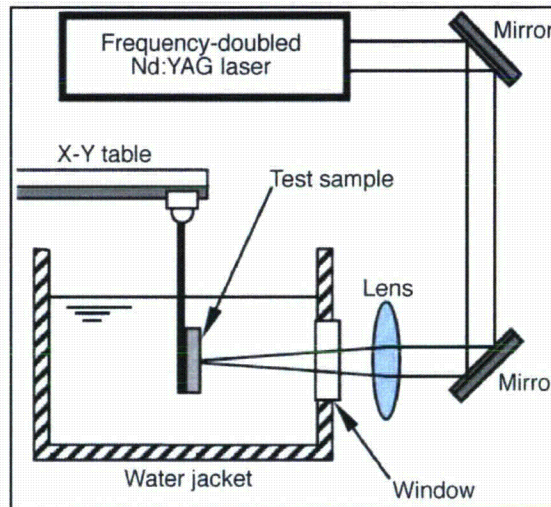


Figure 2-7
Experimental setup of laser peening treatment, by Toshiba

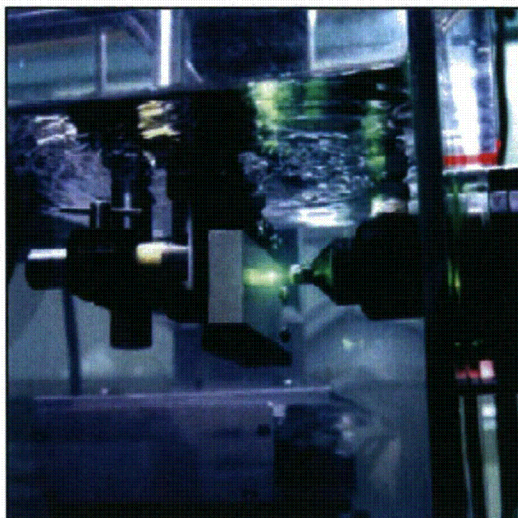


Figure 2-8
Laser irradiation of a test sample immersed in water, by Toshiba

The test samples were prepared from 20% cold-worked Type 304 stainless steel plates. The cold work of 20% simulates the increase of material hardness irradiated in a reactor core region with high-energy neutrons for about 40 years (2×10^{25} neutrons/m², $E_n > 1$ MeV). The typical size of the test sample is 40 mm × 60 mm with a thickness of 10 mm. The central area of 20 mm × 20 mm was irradiated by laser pulses, as shown in Figure 2-9. The samples were preconditioned by grinding work toward the x-direction (parallel to the material rolling direction) to develop a tensile stress on the surface prior to the laser peening treatment.

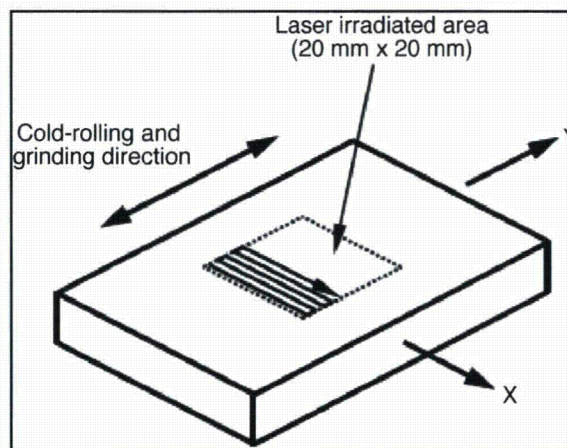


Figure 2-9
Test sample and scheme of laser irradiation, by Toshiba

The surface residual stress was measured at the center of the laser-irradiated area using the x-ray diffraction (XRD) method, where the x-ray beam diameter was about 3 mm. The x-ray source and diffraction plane were a Mn-K α ray and the γ phase (311) plane, respectively. The stress

depth profile was obtained by alternately repeating the measurement and surface layer removal through electrolytic polishing.

A series of experiments was carried out for 20% cold-worked Type 304 stainless steel to obtain the proper extent of laser irradiation conditions, changing parameters such as laser pulse energy, focal spot diameter, and number density of irradiated laser pulses. Figure 2-10 shows a typical depth profile of residual stress in the surface normal direction obtained in the experiment where laser pulses with a pulse energy of 200 mJ were incident on the sample surface with a focal spot diameter of 0.8 mm and pulse number density of 36 pulses/mm². From the comparison of the stress profiles between the laser-irradiated and non-irradiated material, it is evident that the laser peening treatment remarkably improves the residual stress of metal materials.

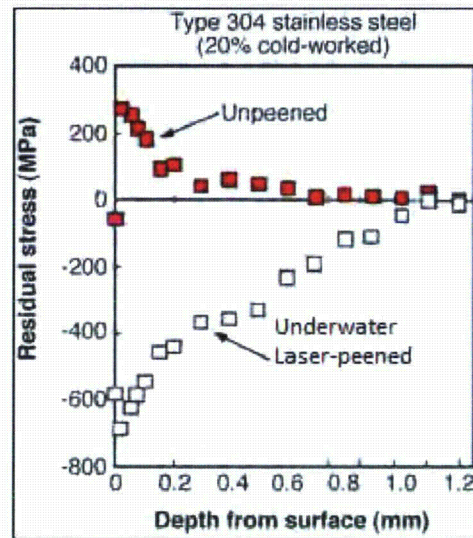


Figure 2-10
Residual stress depth profile on Type 304 stainless steel with and without underwater laser peening, by Toshiba

2.2.2.4 Shock Wave Propagation and Residual Stress

A time-dependent three-dimensional computation was executed for the calculation system, using the plasma pressure as an external force. Figure 2-11 compares the calculated depth profile of the residual stress in the r-direction (σ_r) with the experimental data. The experimental depth profile is fairly well reproduced by the calculation with two or three impacts.

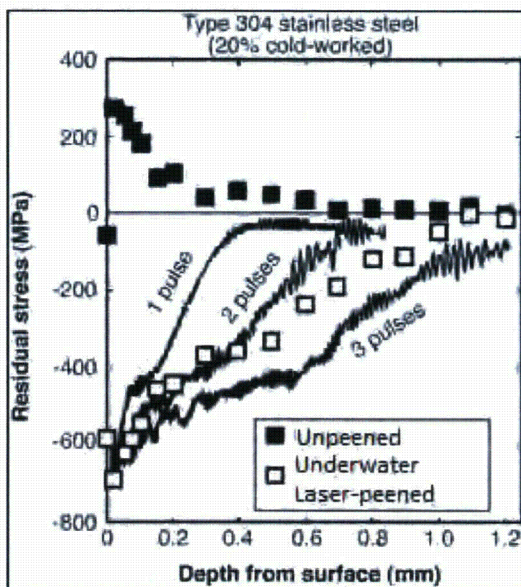


Figure 2-11
Comparison between calculated and measured residual stress profiles, by Toshiba

The stress-improved depth extends incrementally by multiple impacts, based on the assumption that the shock wave propagates as a plane wave and the energy of the shock wave is consumed only by the plastic deformation of the material. In the experiment, the test sample was irradiated by laser pulses with a focal spot having a diameter of 0.8 mm and a pulse number density of 36 pulses/mm². Under this condition, each point on the test sample experiences 18 laser pulses. The corresponding calculation with 18 pulses produces a much deeper stress-improved depth than the 1 mm obtained in the experiment. This discrepancy can be attributed to the plane wave approximation in the calculation model, which could not take account of the three-dimensional dispersion effect in the shock wave propagation.

2.3 Water Jet Peening (WJP)

2.3.1 Shock Waves During WJP

2.3.1.1 Cavitation Bubbles

To understand the cavitation phenomena during WJP, it is important to define the pressure coefficient. For a steady, single phase flow of a Newtonian liquid of constant density, ρ_L , pressure, $p(x)$, a reference velocity, U_∞ , and reference pressure, p_∞ at location x , the pressure coefficient [20] is defined as:

$$C_p(x) = \frac{p(x) - p_\infty}{\frac{1}{2} \rho_L U_\infty^2} \quad [2-5]$$

It is easy to understand that the pressure coefficient is independent of p_∞ for a given geometry of the macroscopic flow boundaries. Unless the reference speed is zero, there will be some location, x_i , where C_p and p are a minimum, whose value can be denoted for convenience by C_{pmin} (note that this is a negative number). It has been pointed out [20] that for a given geometry, $C_p(x_i)$ and C_{pmin} are functions only of Reynolds number in steady flows of viscous liquid.³ While in the idealized inviscid, frictionless liquid, Bernoulli's equation can be applied, and $C_p(x_i)$ and C_{pmin} depend only on the geometry of the flow boundaries. The value of C_{pmin} for a single-phase flow can be generated from either experimental measurement or theoretical calculation.

If the flow velocity is increased so that the pressure at some point in the flow approaches the vapor pressure p_v of the liquid at the reference temperature of T_∞ , cavitation will happen. The cavitation number, σ , is defined below as a measure of cavitation intensity.

$$\sigma = \frac{p_\infty - p_v(T_\infty)}{\frac{1}{2} \rho_L U_\infty^2} \quad [2-6]$$

Any flow has a value of σ , no matter whether it is cavitating or not. The flow will be single phase liquid if σ is sufficiently large. However, as σ reduces, nucleation will first occur at some particular value of σ called the incipient cavitation number. Further reduction of σ below the incipient value causes an increase in the number and extent of vapor bubbles. In the idealized fluid flow that cannot withstand any tension, vapor bubbles appear instantaneously when p reaches p_v or $\sigma = -C_{pmin}$; thus the incipient cavitation number could be identified from the measurements of single-phase flow. In summary, no cavitation bubble will occur for $\sigma > -C_{pmin}$. For $\sigma < -C_{pmin}$ the fluid nucleus experiences $p < p_v$ for a finite time, and thus the vapor bubbles will appear and grow. For $\sigma = -C_{pmin}$ the nucleus occurs at $p = p_v$ only for an infinitesimal moment, so a balanced cavitation is not possible. The rate of growth of a bubble can be greatly affected by the composition and the thermodynamic properties of the liquid and vapor. A detailed discussion is outside the scope of this document.

The discussion of cavitation above is confined to ideal, steady fluid flows. When the flow is assumed to be inviscid, the value of $-C_{pmin}$ is a simple positive constant for a given flow geometry. However, when the effects of viscosity are included, C_{pmin} will be a function of Reynolds number.

2.3.1.2 Bubble Development and Collapse

In order to understand bubble behavior due to cavitations, the application of bubble dynamics is required for deriving the bubble growth and collapse. A single bubble dynamics equation was introduced by Rayleigh in 1917 [21] and further derived by Plesset in 1949 [22]. The generalized Rayleigh-Plesset equation for a traveling cavitation bubble is illustrated below without considering evaporation and condensation:

³ The Reynolds number can be defined for a number of different situations where a fluid is in relative motion to a surface. These definitions generally include the fluid properties of density and viscosity, plus a velocity and a characteristic length or characteristic dimension.

$$\frac{p_b(t) - p_\infty(t)}{\rho_L} = R \frac{d^2 R}{dt^2} + \frac{3}{2} \left(\frac{dR}{dt} \right)^2 + \frac{4\nu_L}{R(t)} \frac{dR}{dt} + \frac{2S}{\rho_L R(t)} \quad [2-7]$$

where R is the traveling bubble radius, S is surface tension, and ν_L is the kinematic viscosity of fluid. This equation can be solved to find $R(t)$ and bubble growth rate dR/dt provided $p_\infty(t)$ and the pressure $p_b(t)$ inside the bubble are known.

Other important parameters for cavitation bubbles are bubble critical size R_c and bubble collapse time t_{cl} . All bubbles of radius $R < R_c$ can exist in a stable equilibrium, whereas the bubbles of radius $R > R_c$ are unstable. An approximation of critical bubble size is given in [20], as shown in the following equation:

$$R_c \approx \frac{\kappa S}{\rho_L U_\infty^2 (-\delta - C_{pmin})} \quad [2-8]$$

where C_{pmin} is the minimum pressure coefficient in the flow and the factor κ is close to unity. An estimated bubble growth or collapse time was derived by Rayleigh by neglecting both the surface tension and the gas content, as described in Equation [2-9]. The t_{cl} represents the time required for a total collapse from R_0 to 0:

$$t_{cl} = 0.915 \left(\frac{\rho_L R_0^2}{p_\infty - p_v} \right) \quad [2-9]$$

It is important to emphasize that the above result has simplified the bubble collapse procedure by neglecting its thermal effects. It was also based on two other assumptions that may be violated during collapse: liquid incompressibility and spherical symmetry. Experimental measurements have demonstrated that the bubble collapse time may be much less than that predicted by the above equation ([20], [23]).

In uncontrolled cavitation, the collapse of cavitation bubbles can cause pitting erosion damage to the surface of materials by emitting a significant acoustic shock wave and macrojet. There is still a lack of agreement regarding which mechanism causes the surface damage ([20], [24]). As indicated in Equation [2-10], the pressure pulse exhibits approximately geometric attenuation as it propagates away from the bubble. It appears that, in most cases, the pressure pulse induced shock wave radiated into the liquid has a peak pressure amplitude of p_p given roughly by:

$$p_p \approx \frac{100 R_{max} P_\infty}{r} \quad [2-10]$$

where the R_{max} is the maximum radius of the bubble and r is the distance to the center of the bubble. This equation gives the order of magnitude of the strong shock wave, which might impinge on a solid surface a few radii away. The equation has been demonstrated experimentally

by Fujikawa and Akamatsu [25]. It should be noticed that much higher pressures will be momentarily experienced in the gas of the bubble ([20], [22], [24]) in the process of collapse. An assumption of spherical symmetry is made in deriving the approximated pressure peak; an off-spherical bubble will cause more violent bubble collapse.

Another dominant feature in the collapse of many vapor bubbles is the development of a reentrant jet due to an asymmetry such as the presence of a nearby solid boundary. Such an asymmetry causes one side of the bubble to accelerate inward more rapidly than the opposite side, which results in the development of a high-speed reentrant microjet penetrating the bubble.

The pressure generated by the macrojet due to a bubble collapse with speed v directly striking a solid boundary is given by the water hammer equation below [26].

$$P_{jet} = \rho_L C_L v \left(\frac{\rho_s C_s}{\rho_L C_L + \rho_s C_s} \right) \quad [2-11]$$

where ρ_L and ρ_s are liquid and solid densities and C_L and C_s are the sound speeds. The jet speed has been experimentally measured to be about 130 m/s or higher [26].

2.3.2 WJP Surface Treatment Technologies and Principles of Operation

The WJP process is built around the concept of producing cavitations in a submerged water jet. Figure 2-12 shows a schematic of the process as it might apply to a flat plate. When a high-speed water jet is produced underwater through a nozzle, a strong shear force acts on the boundary between the high-speed jet and the surrounding stationary water due to strong vortices in the flow as well as the induced turbulence. The vortices and turbulence cause the pressure in this zone to drop below the vapor pressure of the water at the application temperature, causing the water to be locally evaporated to form cavitation bubbles. The cavitation bubbles are caught up in the high-speed water flow exiting the nozzle and move forward, continuing to grow. As the flow moves downstream from the nozzle, it expands and the vortex flow begins to diffuse. This causes the pressure of the flow to return to the nominal surrounding pressure, and the cavitation bubbles rapidly to collapse. The collapse of the cavitation bubbles generates a large shock pressure—on the magnitude of 1000 MPa. When this shock pressure is produced at the surface of a metal, it causes local plastic deformation, which ultimately results in a compression force acting at the material surface. This force can reduce or eliminate residual tensile stresses initially present on the metal surface. When the shock wave passes, relaxation of the initial stresses results in compressive residuals. Figure 2-13 shows various configurations of the WJP process for different components of the reactor vessel.

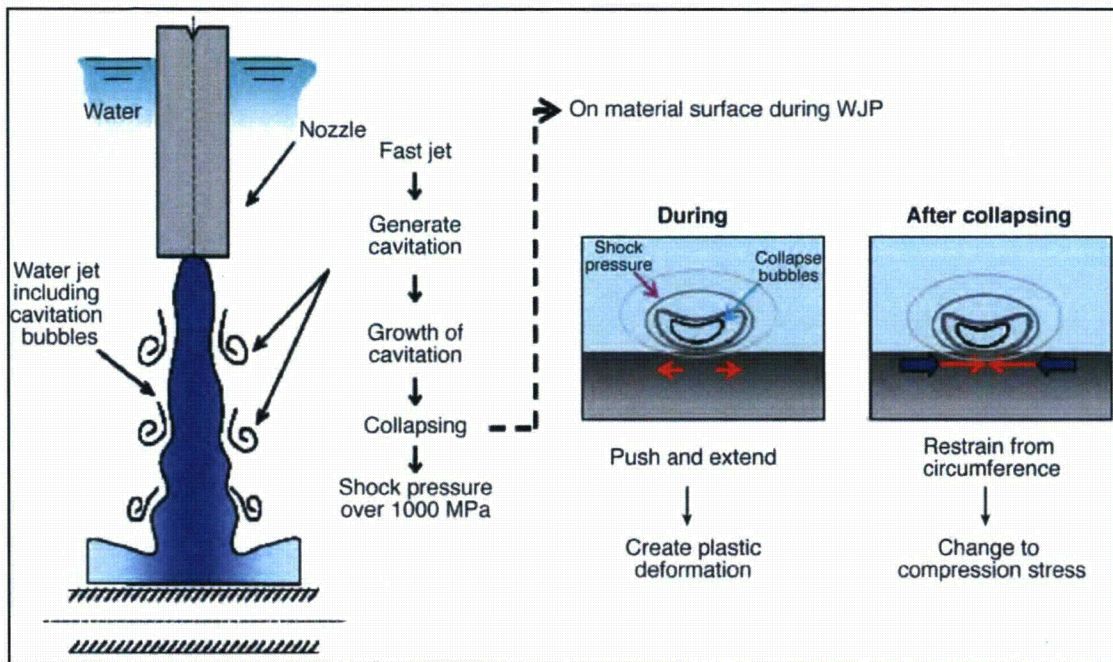


Figure 2-12
Principle of WJP by submerged cavitating water jet, by Mitsubishi

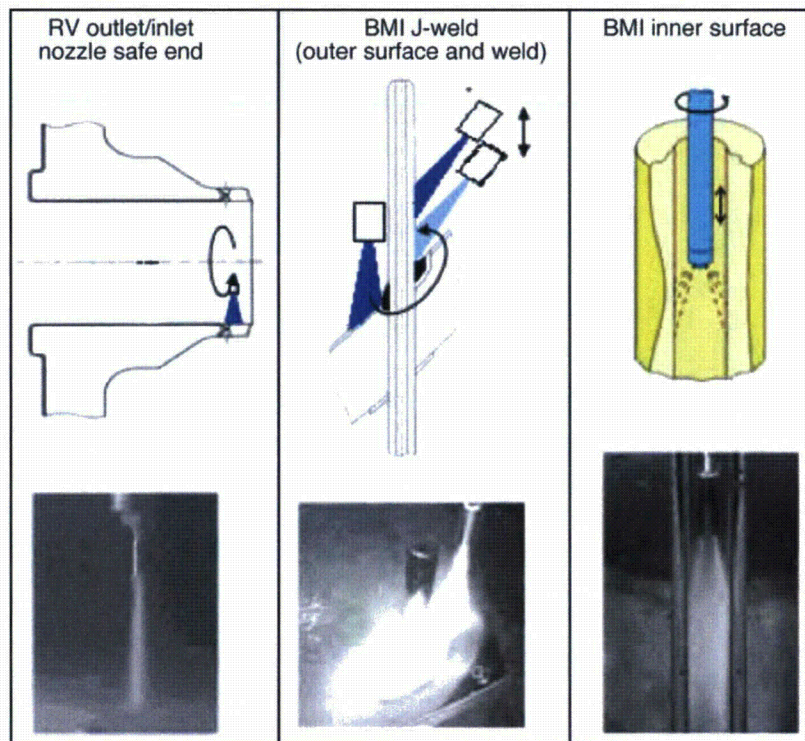


Figure 2-13
Schematic diagrams and photos of the application of WJP to PWR components, by Mitsubishi

By controlling the distance between the WJP nozzle and the metal surface and the angle of the WJP nozzle to the metal surface so that the collapse happens on the metal surface optimally, compressive stress appears on the surface, because plastic deformation generated by the intensive pressure wave is elastically constrained by surrounding metal.

There are several key process parameters that are controlled within defined ranges to ensure that the desired WJP effect is achieved.⁴ The ranges for these control parameters were found by laboratory testing as described in Section 5.3. Extensive testing described in Appendix A shows that through control of these parameters, peening effectiveness is readily achieved while ensuring that material integrity is not compromised.

The basic effect of each key WJP process parameter is discussed below.

2.3.2.1 Nozzle Diameter

The nozzle diameter is an essential parameter in controlling the velocity of the water jet. For a given water pressure and flow rate, a smaller nozzle diameter will give a higher flow velocity. The change in velocity of the jet affects the size of the vortices and the degree of turbulence for the flow, which has a direct influence on the creation of the cavitation bubbles. As the velocity of the flow increases, more cavitation bubbles are created. The creation of more cavitation bubbles causes a greater shock pressure to be induced onto the materials being mitigated, meaning that a greater WJP effect will be realized. The laboratory testing has defined nominal nozzle diameters for each process configuration that work to deliver the required WJP effect.

2.3.2.2 Nozzle Stand-Off

The nozzle stand-off represents the distance from the outlet of the nozzle to the surface of material to be mitigated. The stand-off distance should be controlled in an optimized range in order to spread the flow sufficiently before it impinges on the surface of the component. As the stand-off distance is decreased, the flow will diffuse less, so the cavitation bubbles and the WJP effect will be concentrated on a smaller area. The laboratory testing explored a range of stand-off distances for each configuration of the WJP equipment to define acceptable ranges to ensure that the desired WJP effect is realized.

2.3.2.3 Water Jet to Material Angle

This parameter is related to the stand-off distance. If the nozzle is situated such that the flow is directly impinging on the material surface (perpendicular), then the water jet will diffuse less and the maximum WJP effect will be seen. However, if the angle between the nozzle and the material surface is less than 90°, then the flow will diffuse more and cause the cavitation bubbles to spread over a larger area of the component, thus reducing the intensity of the WJP effect. The laboratory testing defines an acceptable range for the angle to ensure that the desired WJP effect is realized.

⁴ Each peening vendor has performed testing for their process and has determined ranges in which the process can be applied. The established ranges for the control parameters are such that it is feasible to stay within them over the course of peening. The actual values of the control parameters are considered proprietary to the respective vendors.

2.3.2.4 Flow Rate

The flow rate works with the nozzle diameter parameter to control the creation of cavitation bubbles in the flow. For a given nozzle diameter, an increase in flow rate will cause an increase in the number of cavitation bubbles (a smaller cavitation number) that will be created, whereas a lower flow rate will cause fewer cavitation bubbles to materialize. Thus, increasing the flow rate increases the WJP effect that is seen by the materials to be mitigated. The laboratory testing has been used to define an acceptable range for the flow rate for each configuration in order to deliver the desired WJP effect.

2.3.2.5 Application Time

The WJP process is applied using a constantly moving nozzle. The speed at which the nozzle moves is a process control parameter that has an impact on the WJP effect. The longer the application time, the more time one area will be influenced by the cavitation bubbles, thus the greater the WJP effect. The laboratory testing has identified a suitable range of application times such that the desired effect is ensured without surface erosion occurring.

In addition to the five parameters discussed above, the WJP process is affected by two additional parameters as well. Both of these following items are related to the effectiveness of the WJP process.

2.3.2.6 Thickness of the Materials to Be Mitigated

Components that are fabricated from thicker materials (greater than a few millimeters) will see a greater influence from the WJP effect. The compressive residual stresses are created by the WJP process when a small surface layer of the material undergoes plastic deformation. This small plastic deformation only affects the surface of the material, since the unaffected material underneath works to restrain the deformation, which results in a compressive surface layer. If the materials are thin (less than a few millimeters), then the induced stresses at the surface can cause the material underneath the surface layer to deform, thus reducing its ability to restrain the surface deformation. This causes thinner materials to see less effect from the WJP process, compared to thicker materials, when treated using the same configuration with the same process parameters. In practical applications of WJP to RV and other thick-wall PWR components, material thickness is sufficient not only to ensure a sufficient WJP effect on the mitigated surface, but also so that the effect of the peening on increasing tensile stresses below the compressive residual stress zone is rather small.

2.3.2.7 Water Pressure

Water pressure also has an influence on the WJP effect. A higher water pressure will result in a larger shock pressure when cavitation bubbles collapse. This causes the collapsing bubbles to have a greater effect on the surface of the materials being mitigated, meaning that there is a greater effect from the WJP application. In general, the water pressure is defined by the capability of the pumps used in the process. Furthermore, this parameter is related to nozzle diameter and water flow rate, so that in practical applications it does not need to be considered independently.

2.4 Air Laser Peening (ALP)

2.4.1 Technology Introduction

In the air laser peening process a laser beam, typically in the range of 25 J per pulse and 25 ns duration with a resulting peak power of over 10^9 watts, is imaged onto the surface of a material with a spot size in the range of 3 mm to 10 mm and thus irradiances of 11 GW/cm^2 and 1 GW/cm^2 , respectively. As shown in Figure 2-14, a metal component to be laser peened is sometimes covered with a layer of material to function as an ablative source. On top of this layer is flowed a thin, typically 1 mm thick, layer of de-ionized water (approximately $15 \text{ M}\Omega$ resistance). The water is transparent to the $1 \mu\text{m}$ wavelength laser light and is employed not to cool the substrate but to act as an inertial layer (or tamping layer) to momentarily confine the high pressure plasma that forms. Upon firing of a laser pulse, the intense electric field of the high power laser ablates material at the ablation layer, creating a plasma that within nanoseconds reaches temperatures in the range of 16,000 K and lasts for about 2.5 times the laser pulse duration. The plasma would tend to “blow” off the surface of the substrate but is trapped between the substrate and the water layer. The inertial resistance of the 1 mm thick layer of water is sufficient to confine the plasma within a thickness of about $10 \mu\text{m}$ during this time period, enabling the pressure to reach roughly 40,000 atmospheres.

This rapid rise in surface pressure creates a shock wave with pressure above the yield strength of the substrate. The shock wave propagates through the ablative layer and into the metal, plastically deforming it as it propagates inward. The large energy of the laser enables spot sizes of 3 mm to 10 mm depending on the yield strength of the material being peened, thereby creating a plane wave of relatively uniform transverse spatial intensity. The large spot size is an important factor as the plasticity propagates uniformly to depths comparable to its characteristic dimension before evolving into a spherical wave of rapidly falling spatial energy. This high energy approach to air laser peening permits use of a large spot size that generates a pressure wave that is sustained, producing a relatively large depth of plasticity. Thus the ALP approach produces a relatively deep and uniform layer of treated material.

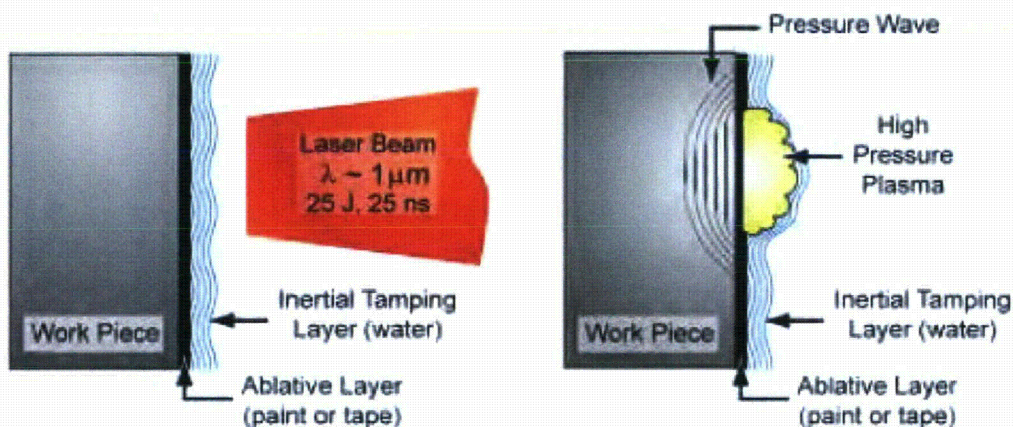


Figure 2-14
Schematic design of air laser peening process showing work piece, ablative layer, inertial tamping layer and laser input, provided by Metal Improvement Company (MIC)

The air laser peening can also be performed without the use of the ablative layer. Processes with and without the use of an ablative layer have been successfully applied in the aerospace industry. In this case the high power beam will ablate a thin layer of the work piece material, and as the plasma cools this material will condense back onto the metal surface, resulting in a recast and thermally impacted layer of about 10 μm thickness. Elimination of the ablative layer results in more rapid and lower cost processing. The effectiveness of ALP mitigation without use of an ablative layer is supported by SCC tests that have been performed using U-bend samples peened without the ablative layer. For nuclear power plant applications, the intention is to apply ALP without the ablative layer due to time and cost considerations.⁵

Air laser peening is essentially a high technology laser hammer that drives deep levels of plasticity into metal surfaces, creating protective layers of compressive stress and thereby mitigating crack initiation and arresting growth of flaws located in the compressive region. Figure 2-15 shows an example of the much greater depth of compressive stress generated by ALP as compared to conventional shot peening in Aluminum 7050 T7451. The contrast between depth of compression with shot peening and air laser peening is characteristic of numerous materials, including the nickel-based alloys used in nuclear power plant components. In the legend and throughout this section, a "callout" consisting of three values separated by hyphens indicates the laser parameters used during peening: the irradiance in GW/cm^2 , the pulse duration in ns, and the number of full coverage layers. In this case, "4-18-3" corresponds to an irradiance of 4 GW/cm^2 with a pulse duration of 18 ns and 3 full layers applied.

Figure 2-16 shows results of air laser peening Alloy 22, a highly corrosion resistant nickel-based alloy chosen as a candidate for nuclear waste disposal. As shown, in this case the ALP process produces a greater than 4 mm (0.160 inch) deep layer of compressive residual stress in this material.

⁵ As discussed in Section A.1.1.3 of Appendix A, the stresses developed by LSP without an ablative layer are tensile at the surface but rapidly decrease to highly compressive values within about 35 μm . The stresses then remain compressive until at least a depth of 1.5 mm. The underlying high compressive stresses act to inhibit formation of significant cracks at the surface.

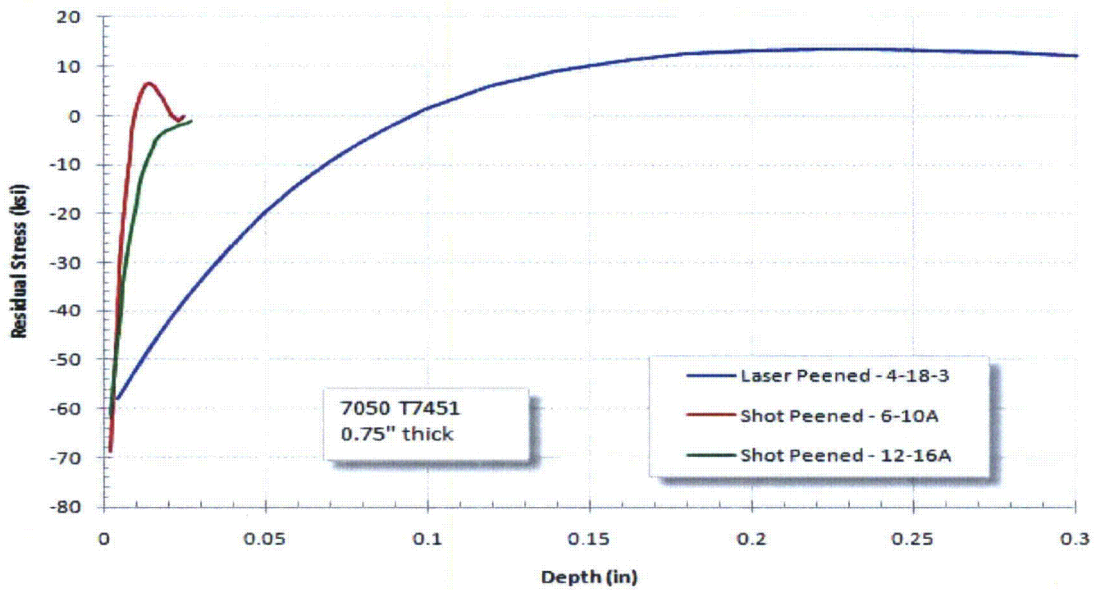


Figure 2-15
Residual stress profiles as a function of depth for an aluminum alloy (Al 7050 T7451) treated with ALP and shot peening (SP), provided by MIC

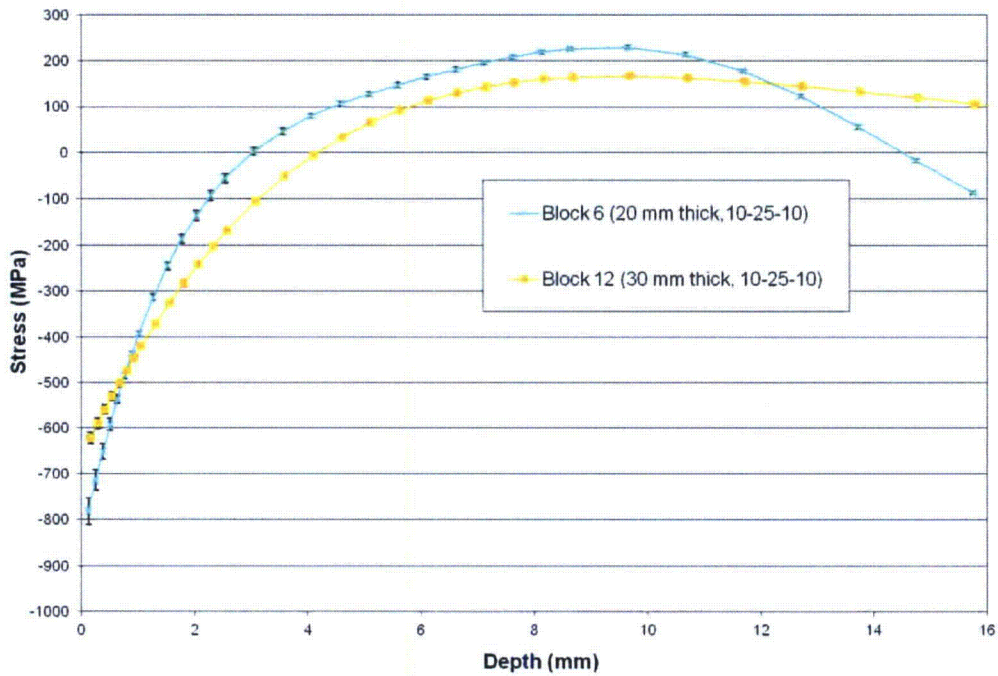


Figure 2-16
Example of compressive residual stress profile for air laser peening of nickel-based Alloy 22, provided by MIC

Figure 2-17 shows the results of a stress corrosion cracking test performed using ALP on butt weld geometries made of 316 stainless steel. In this experiment, a butt weld was performed along the entire width of the sample, and the area indicated by the white hashed block in Figure 2-17 was laser peened while the other areas were not treated. Then, two cut off glass flasks were epoxied onto two sections (the black circles comprise the epoxy and glass remnants) that encompassed portions of the welds. Each flask was then filled with a magnesium chloride solution ($MgCl_2$), heated to the solution boiling point ($155^\circ C$), and held at this temperature. As can be seen below, stress corrosion cracks developed in the unpeened region and cracked the sample transverse to the weld and longitudinally along the heat affected zone running up to the compressive stress field developed by the air laser peening where the cracks arrested. The laser peened region was free of stress corrosion cracks and had less signs of overall corrosion.

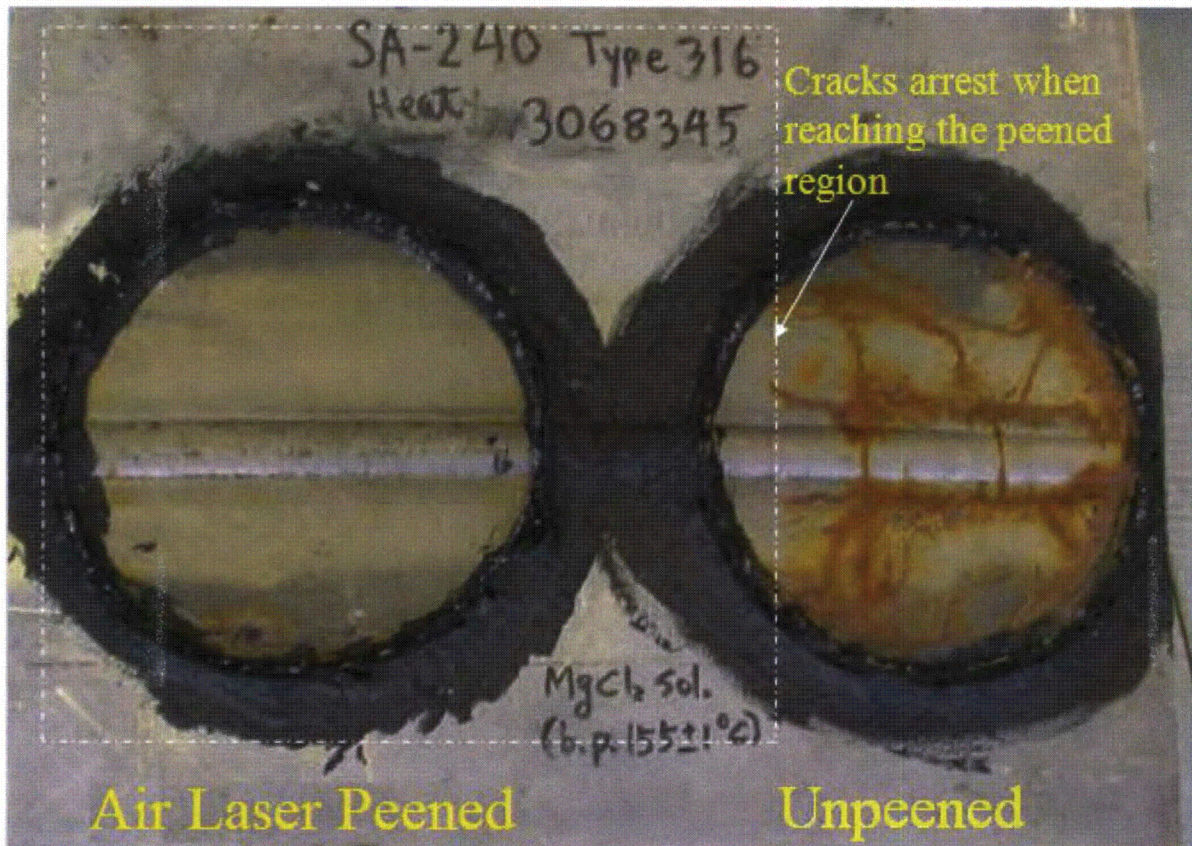


Figure 2-17
Results of SCC testing performed with ALP on a butt weld geometry for Type 316 stainless steel material, provided by MIC

2.4.2 Experimentally Measured Stress Profiles in ALP Treated Specimens

This section includes additional experimentally measured residual stress profiles of Alloy 22 specimens treated with ALP. These results are used to investigate the stress state induced on components treated with ALP, both at the surface and deep into the volume, and the effect of multiple peening layers on the residual stress state of the treated component.

ALP is not expected to generate tensile residual stress on a peened surface with proper peening of a surface area. However, an area that is in a state of tensile stress before laser peening and is left unpeened could remain in a state of tensile stress. ALP does not directly generate compressive or tensile stress; it induces plastic yielding normal to the surface, and the plastically compressed material transversely expands in order to conserve volume. The response of the surrounding material generates stress and strain. Tensile stresses tend to be generated by the local material bending moment that is created in response to the elongation of the surface. The stresses associated with the bending moment (tensile above the centroid and compressive below) sum with the compressive layer generated by the compression response of the surrounding material to form the overall stress profile. Figure 2-18 below, shows a residual stress curve for laser peening of a 20.8 mm thick coupon of Alloy 22. The linear portion of the right hand side of the curve and the transition from tensile to compressive stress is indicative of the bending of the coupon. For a thicker coupon the slope of the bending moment would be smaller as would be the maximum tensile stress generated (remember that this tensile stress is 4 mm beneath the surface). For an infinitely thick coupon, the peak tensile stress would tend toward zero and the depth of this peak stress would be at approximately 10 mm depth into the sample.

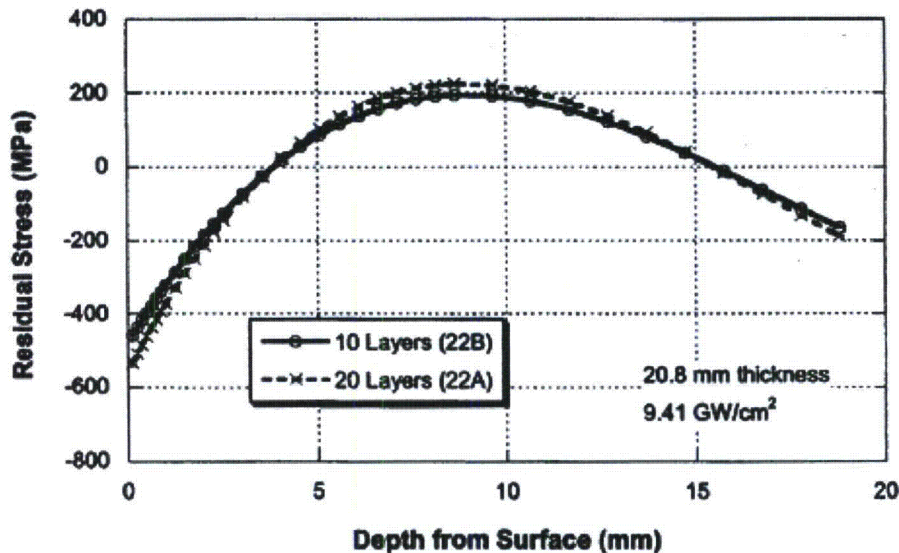


Figure 2-18
Residual stress versus depth as a function of number of peening layers in 20.8 mm thick coupons of nickel-based Alloy 22, provided by MIC

MIC compared the effect of treating an Alloy 22 weld with ALP by comparing stress profiles of a peened weld with an unpeened weld. The stress profiles shown in Figure 2-19 represent two-dimensional contour stress profile measurements in a peened weld and an unpeened weld. The results from the figure show that tensile stresses were converted into compressive residual stresses to a depth of at least 0.06 in (1.5 mm).

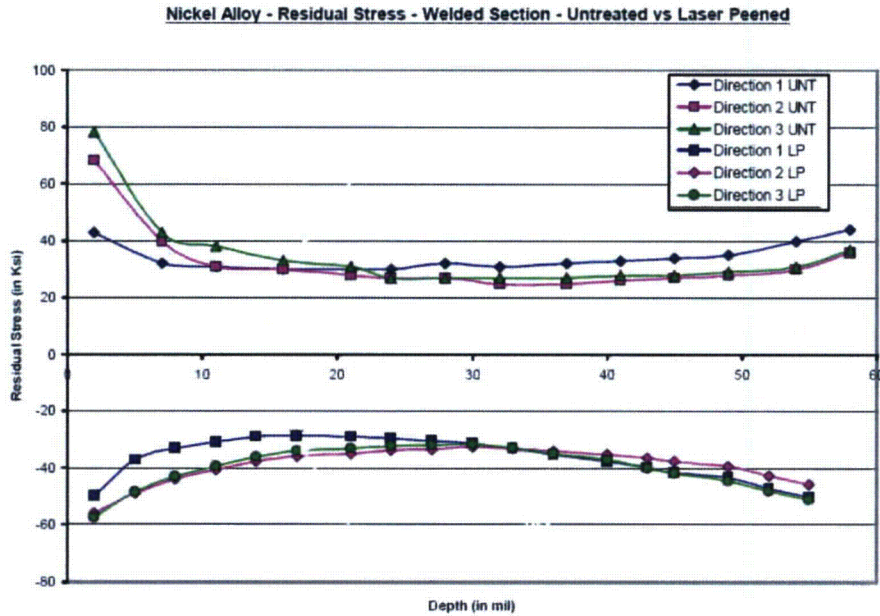


Figure 2-19
Residual stress profiles for ALP treatment of a nickel-based Alloy 22 weld, provided by MIC

The effects of air laser peening were evaluated by the Lawrence Livermore National Laboratory (LLNL) and the University of California at Davis in actual Alloy 22 weldments using samples fabricated from a butt-welded 33 mm (1.3 inch) thick Alloy 22 plate, D-22 (HT 059902CL1, welded by Framatome Technologies Inc.). The initial plate was approximately 813 mm (32 inch) long (longitudinal) and 201 mm (7.9 inch) across (transverse). This plate was cut into four 190 mm (7.5 inch) long, full-width samples, and two of these were used in this work. Air laser peening was applied to one surface of one sample. The peened region was centered on the weld and was 76 mm (3 inch) long and 100 mm (4 inch) wide. The cutting of the specimens was performed on a Sodick AQ325L linear motor driven wire EDM by a commercial vendor, and measurement of the cut surfaces was performed on a high-precision Leitz PMM 12106 coordinate measuring machine (CMM) at LLNL.

Longitudinal residual stress profiles as a function of depth from the surface in peened and unpeened welds are shown below for three different locations in the weld: at the center of the weld bead (Figure 2-20), at the right weld toe (Figure 2-21), and outside of the welded region (30 mm (1.2 inch) from the weld center, (Figure 2-22). These plots clearly show the effect of air laser peening and indicate that it produces deep compressive stress in both weld and base metals and at the geometrically discontinuous weld toe.

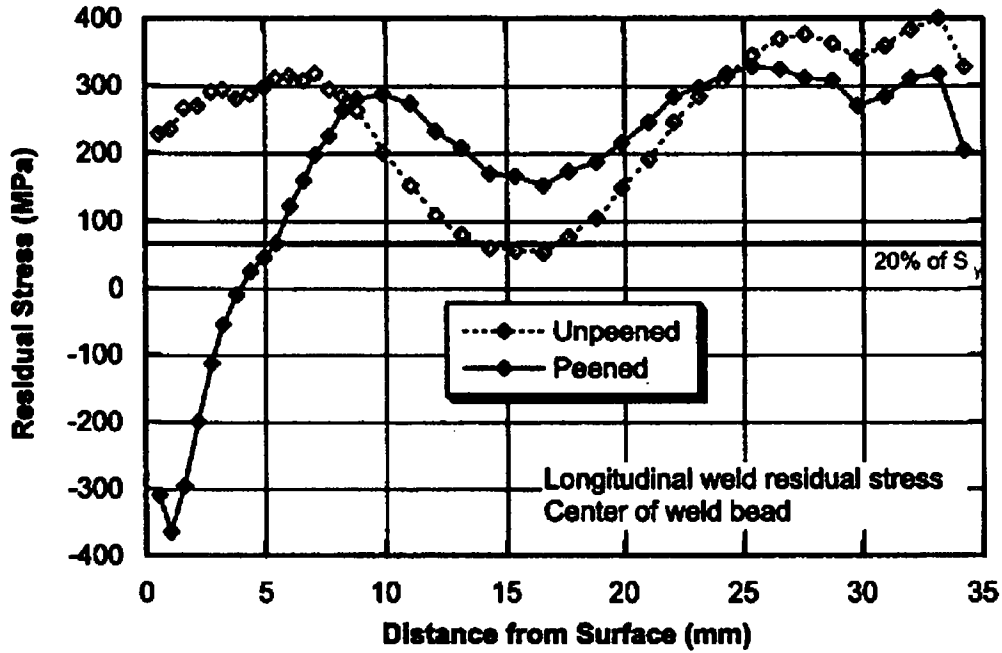


Figure 2-20
Longitudinal component of residual stress at the center of the weld bead with and without air laser peening (Alloy 22), provided by MIC

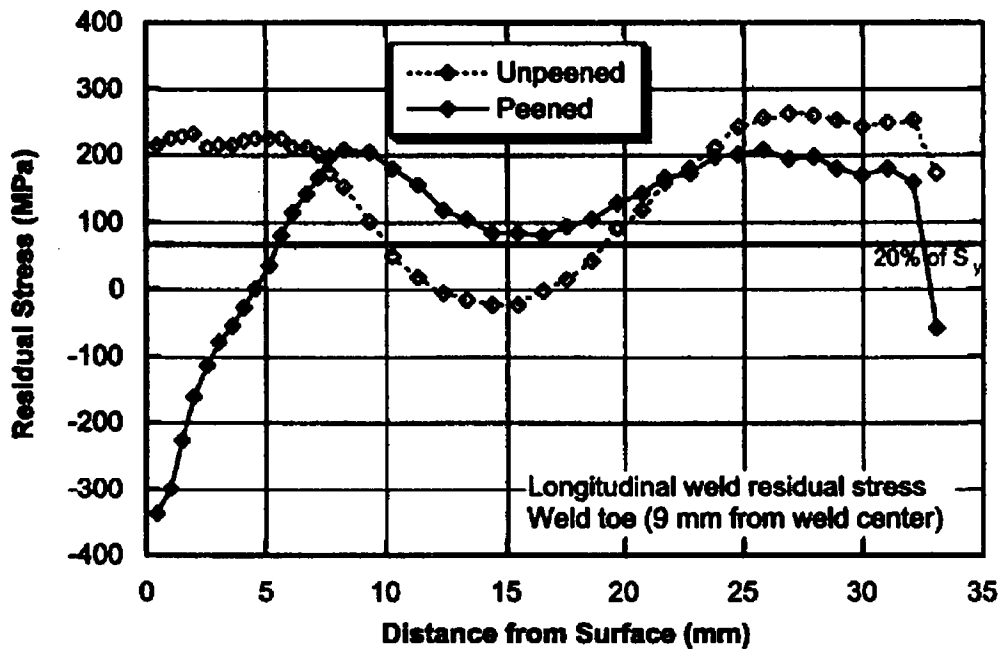


Figure 2-21
Longitudinal component of residual stress at the right weld toe, with and without air laser peening (Alloy 22), provided by MIC

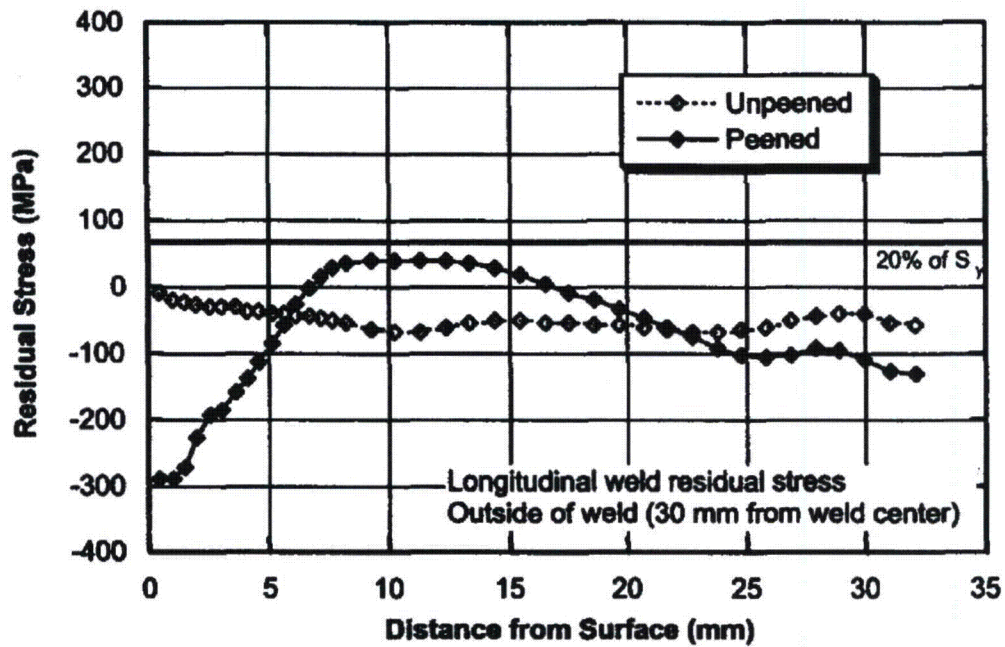


Figure 2-22
 Longitudinal component of residual stress outside the weld region (30 mm from the weld center) with and without air laser peening (Alloy 22), provided by MIC

The difference in the longitudinal weld residual stress between corresponding peened and unpeened regions in the welds is shown in Figure 2-23. The differences were calculated from the data plotted in Figure 2-20 to Figure 2-22. The stress differences indicate that laser peening has a larger effect in regions of initially tensile weld residual stress. The region outside the weld but still laser peened shows reduced compressive stress on the surface, but the depth of compression is essentially equal. This may be due to the effect of initial weld residual stress on plastic deformation induced by laser peening, or by a limit to the maximum level of compressive stress that can be introduced by laser peening. The latter possibility is supported by the fact that the maximum compressive residual stresses in Figure 2-20 to Figure 2-22 are nearly equal.

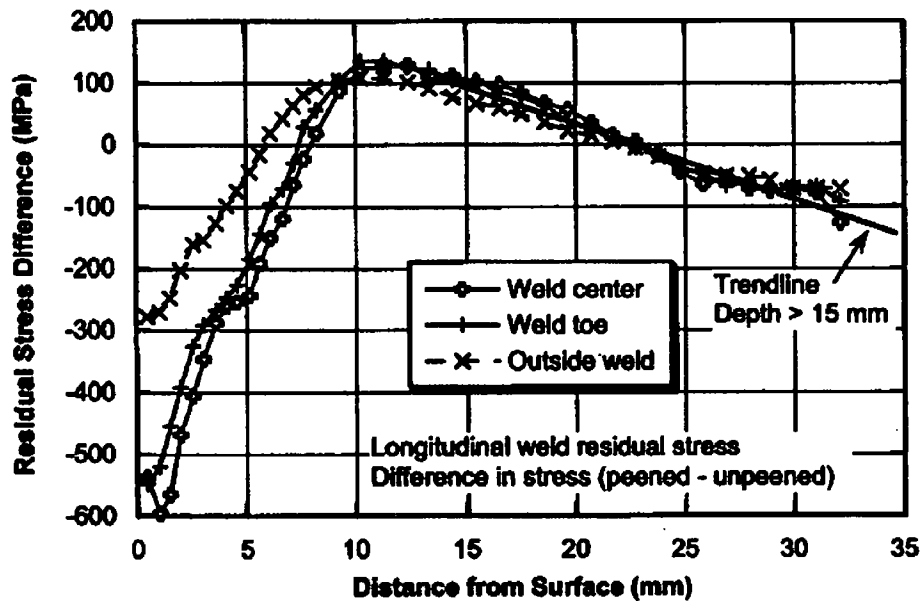


Figure 2-23

Difference between the longitudinal component of residual stress in air laser peened and unpeened weld samples, at various positions transverse to the weld (Alloy 22), provided by MIC

MIC has evaluated two potential sources of “over-peening” a surface: the number of peening layers or the production of an excessively energetic shot. The peening process has been shown to saturate with multiple layers of peening. It is proposed that acceptable peening will be achieved with 3 layers of coverage for PWRs. Figure 2-24 below shows that 5 layers of peening gives slightly greater residual stress than 2 layers of peening, but increasing the number of peening layers to 10 does not appreciably change the stress profile. This result in a material with a thickness of 9 mm shows that the anticipated stress profile in thin material is influenced by the ability of the component to strain by bending.

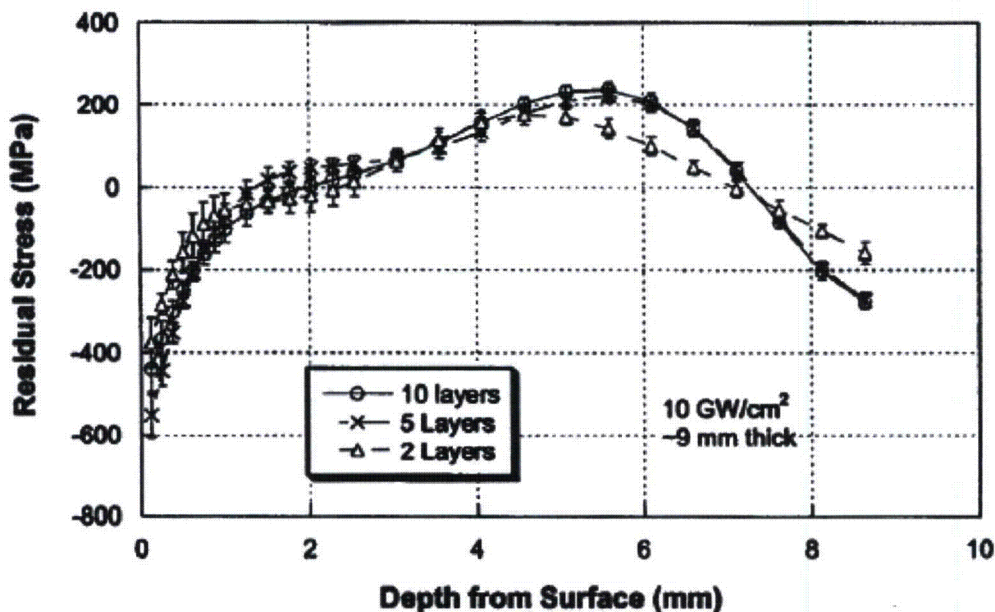


Figure 2-24
Residual stress versus depth as a function of number of peening layers in 9 mm thick coupons of nickel-based Alloy 22, provided by MIC

Another possible source of over-peening is an excessively energetic laser shot. It has been determined that the material being subjected to ALP is protected from this by several mechanisms. First of all, the breakdown potential of the tamping layer of water, which is used in the processing, is about 14 GW/cm^2 which is only 40% above the nominally proposed peening level. Thus if a shot were to occur with excessively high power density, called irradiance, the water would breakdown and prevent the peening from occurring. A rectification pulse can then be added. Also the pressure increase scales as the square root of the irradiance so the difference in peening pressure between 10 GW/cm^2 and 14 GW/cm^2 would only be 25%. Another mechanism that protects the process from an energetic shot is the saturation mechanism within the laser and the control on the power supply. The laser output energy is governed by the energy input to the glass amplifier by flash lamps driven by a power supply. If the power supply were to unexpectedly output excessive energy, the flash lamp energy would increase and pump the glass gain medium to a higher gain. Since we multi-pass the amplifier eight (8) times and have tailored the amplifier input and gain to reach saturation on the eighth (8th) pass, the amplifier will saturate somewhat on an earlier pass and lose some of the excess energy.

2.4.3 Current Commercial Applications of ALP

By inducing compressive stress, the laser treatment enhances the fatigue lifetime of commercial components. Over 40,000 commercial jet engine blades, aircraft structural parts, and commercial gas and steam turbine blades have been treated using ALP. The treated components last 10 or more times longer in fatigue, saving hundreds of millions of dollars in replacement parts, reducing system inspections and overhauls, and increasing availability for airlines and power generation companies. Examples of deployment of air laser peening on commercial systems include jet engine fan blades for the Boeing 777 and 787, Gulfstream V and VI, and Airbus

A340 aircraft; gas and steam turbine blades for companies such as Siemens; and automotive tooling for reduced tooling failure and more efficient manufacturing.

In the military, ALP is being deployed to extend the lifetime of the wing attachment lugs for the F-22 fighter jet, eliminating a serious and potentially costly fatigue failure. In another example, the ALP technology is undergoing final qualification testing for deployment on the arrestment hook shanks of the Navy's T-45 trainer (Figure 2-25), which is a very high stress application. There is a large benefit of ALP of these components as shown in Figure 2-26, which plots the probability of failure for tests with representative unpeened, shot peened, and air laser peened samples.



Figure 2-25
T-45 arrestment hook shank

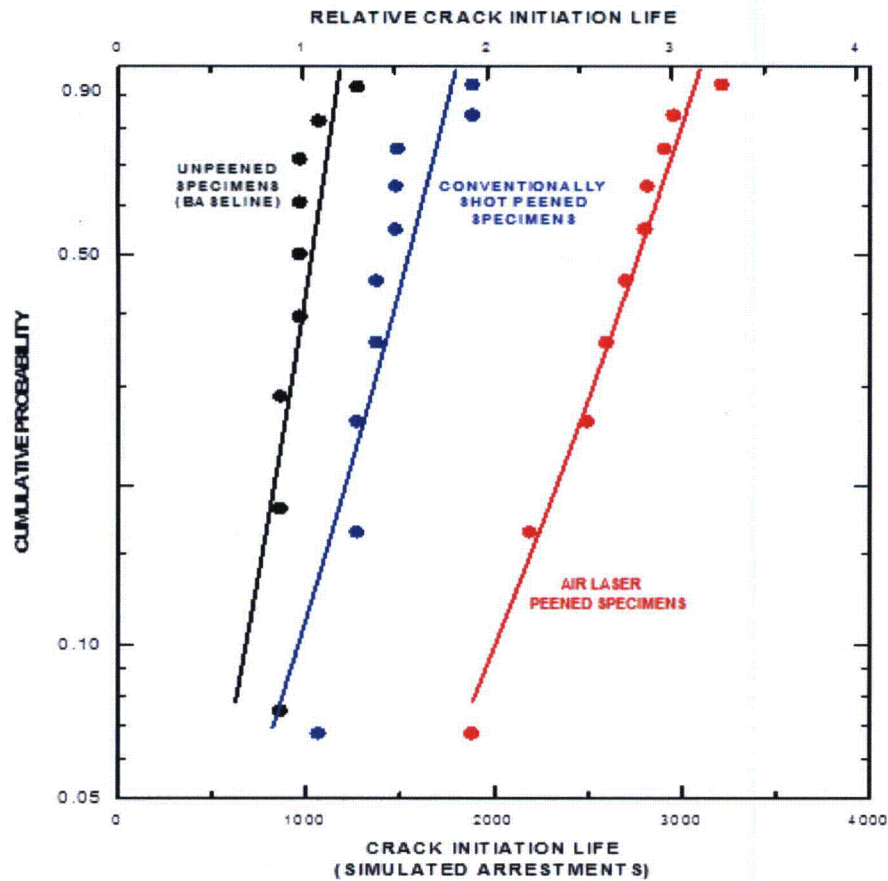


Figure 2-26
Results of fatigue crack testing of unpeened, shot peened, and air laser peened T-45 arrestment-hook-shank-like samples, provided by MIC

In the last three years, the ALP process has also been used to precisely form the thick section of wing skins of Boeing's new 747-8 heavy aircraft, facilitating its advanced wing curvature design. This precision forming application helps make this aircraft the world's most fuel efficient passenger jet.

Figure 2-27 shows an example of the effectiveness of air laser peening to eliminate SCC in 300M steel used for aircraft landing gear. The steel samples in these tests treated by ALP did not crack after more than 1500 hours of exposure to a high tensile stress of 180 ksi (1240 MPa) and a corrosive atmosphere.

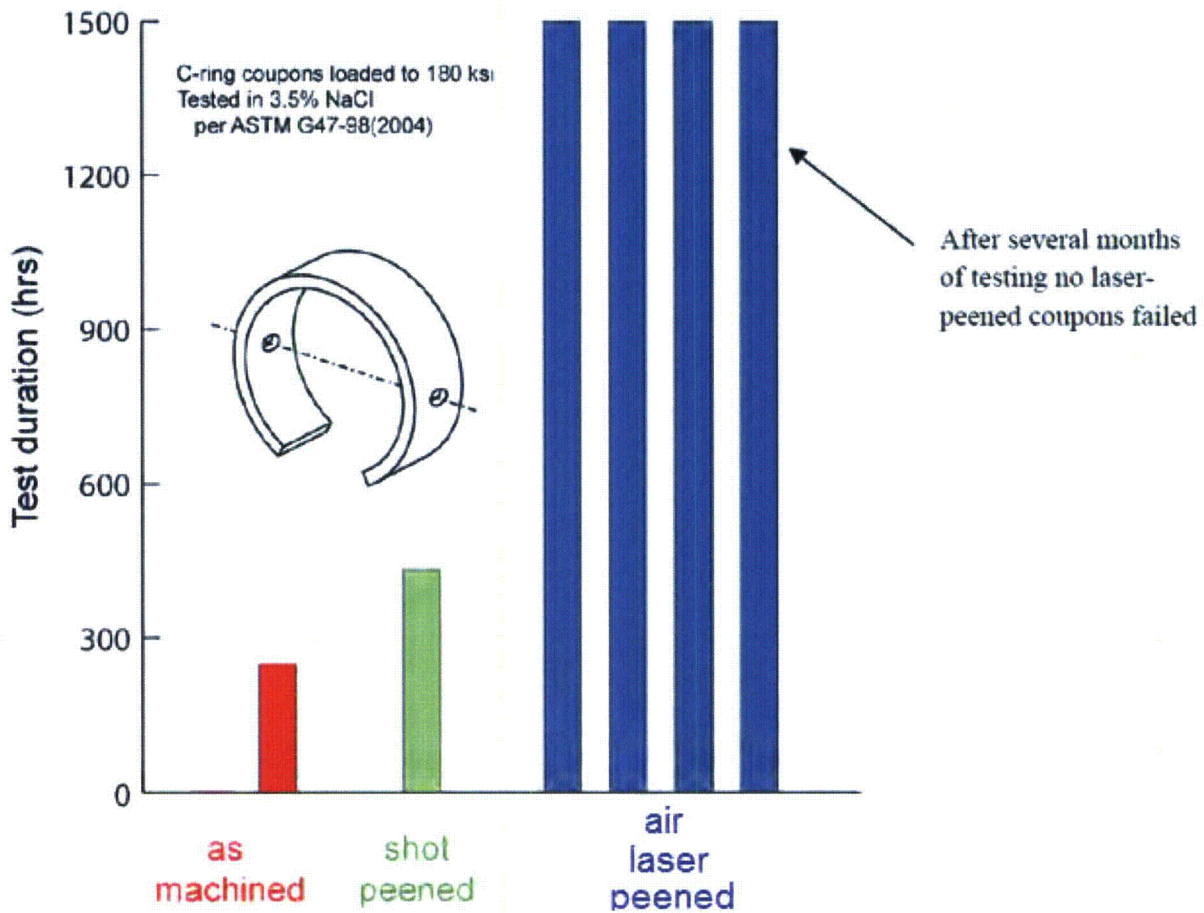


Figure 2-27
Results of SCC tests of unpeened, shot peened, and air laser peened 300M steel C-ring coupons prepared according to ASTM G47-98, provided by MIC

2.4.4 MIC Air Laser Peening (ALP) System

The MIC approach to laser peening uses a high-energy laser system that can be brought to a customer site in a completely self-contained trailer. High beam quality allows the beam to be delivered from a remote location, and an advance beam scanning system is used to accurately register the treatment patterns over complex surfaces of the work piece and accurately apply the high energy laser pulses. As discussed in Section 5.4, a straightforward adaption of this proven beam delivery system will allow laser peening spot patterns to be applied to the outer surface of RPVHPNs in PWRs.

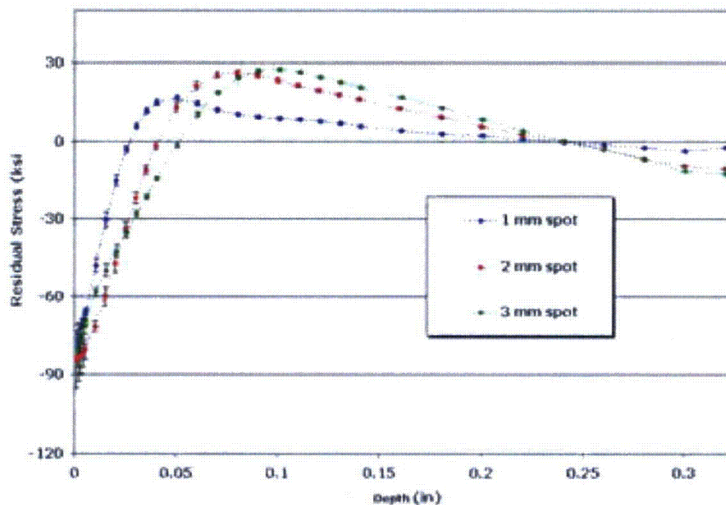
The laser system is based on technology originally developed in the Laser Program at Lawrence Livermore National Laboratory (LLNL) and licensed for exclusive applications of air laser peening by MIC. Over the past 10 years, the advanced LLNL design has been transformed by MIC into robust, reliable, and transportable devices that can be located and operated on-site at customer facilities. MIC has 10 laser systems located in four laser peening processing plants around the world with a fifth plant going online in 2012. The lasers are commercially proven tools and available up-times have exceeded 97%.

2.4.4.1 Beam characteristics

The MIC system uses a laser system with an output optimized for efficient, high-throughput commercial air laser peening with relatively deep levels of compressive stress. The output beam is comprised of high-energy pulses to optimize depth of laser peening plasticity, has adjustable pulse duration to tailor the laser peening effect to each application, delivers square spots for optimal coverage and surface quality, and has high beam-quality for beam delivery across extended distances.

2.4.4.1.1 Pulse energy

The MIC laser system generates a high-energy pulsed laser beam with a peak power of up to 1 GW. This allows large spots (2.5-10 mm squares) to be illuminated with power densities of up to 10 GW/cm². As discussed above, the large spot size produces deep levels of plastic deformation with corresponding deep compressive residual stress. Large pulse energies of up to 25 J/pulse can be delivered with a pulse repetition frequency (PRF) of up to 5 Hz, at least 5× faster than any other laser system in this pulse-energy class. As shown in Figure 2-28, the depth of plasticity is increased by over 2× for a single layer of treatment when the incident pulse energy is increased from 1.8 J/pulse to 16 J/pulse, with the spot size adjusted to deliver a constant power density on the work piece.



- **Ti 6-4 test blocks air laser peened at 10-18-2 show a >2X increase in depth of plasticity from 1mm to 3mm spot size**

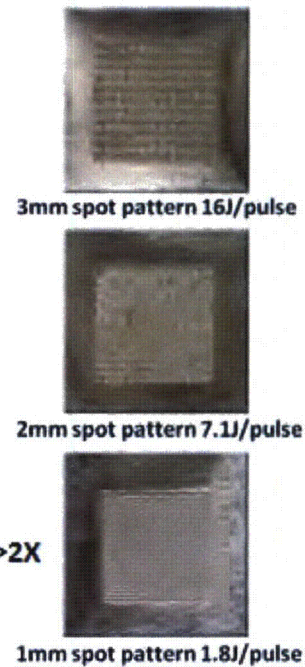


Figure 2-28

Comparison of residual stress profiles for laser spot sizes ranging from 3 mm to 1 mm square at a fixed power density of 10 GW/cm² (titanium alloy samples), provided by MIC

2.4.4.1.2 Pulse width

The duration of each laser pulse, often referred to as the pulse width, is a critical process parameter. As such, the laser system allows the parameter to be adjusted over the range between 9 and 30 ns as shown in Figure 2-29. The width of the laser pulse allows the depth of compressive residual stress and the resulting distribution of sub-surface compensating tensile stress to be controlled based on component geometry and metal alloy. The longest laser pulses produce the deepest compressive residual layer, while a shorter laser pulse allows the plastic depth to be reduced while still maintaining a significant compressive stress at the surface.

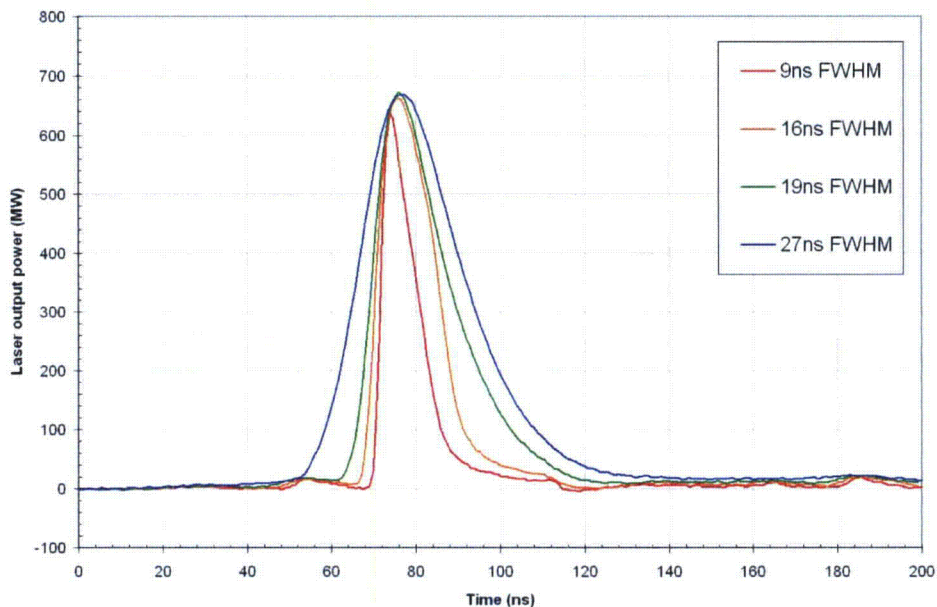


Figure 2-29
Comparison of laser output pulse shapes for widths of 9 to 27 ns, provided by MIC

2.4.4.1.3 Laser spot shape

The architecture of the MIC laser system gives it a square output beam compared to the large majority of other laser systems which have a round (circularly symmetric) beam. Rather than being peaked in the center, the MIC beam has a near-flat irradiance profile, providing highly uniform peening pressure over the entire footprint on target. This is beneficial to the laser peening process, allowing laser peening treatment spots on the work piece to be accurately placed, side-by-side, in a uniform pattern such as that shown on the test blocks in Figure 2-28. It also provides 100% coverage in a single layer of laser peening, without the need to strongly overlap spots. The result is a good surface finish (R_a of ~64 microinches (1.6 μ m)) and a highly uniform residual stress field. The system has the capability to carefully track the level of laser peening coverage received by each location on the work piece, facilitating the monitoring of the process for quality assurance.

The output from the beam delivery system that carries laser pulses from the laser system to the beam scanning tool is a 32 mm (1.25") square beam. Before being applied to the work piece, this beam is reduced to a spot usually ranging from 2.5 to 10 mm. The beam reduction is made using

a patented optical system that places a demagnified image of the output aperture of the laser system onto the treatment surface, eliminating distortions that could arise from optical diffraction and wave front distortion using a conventional beam focusing system. Pattern generation software allows the square spots to be arrayed over numerical meshes that follow complex surfaces on the work piece, as illustrated in Figure 2-30.

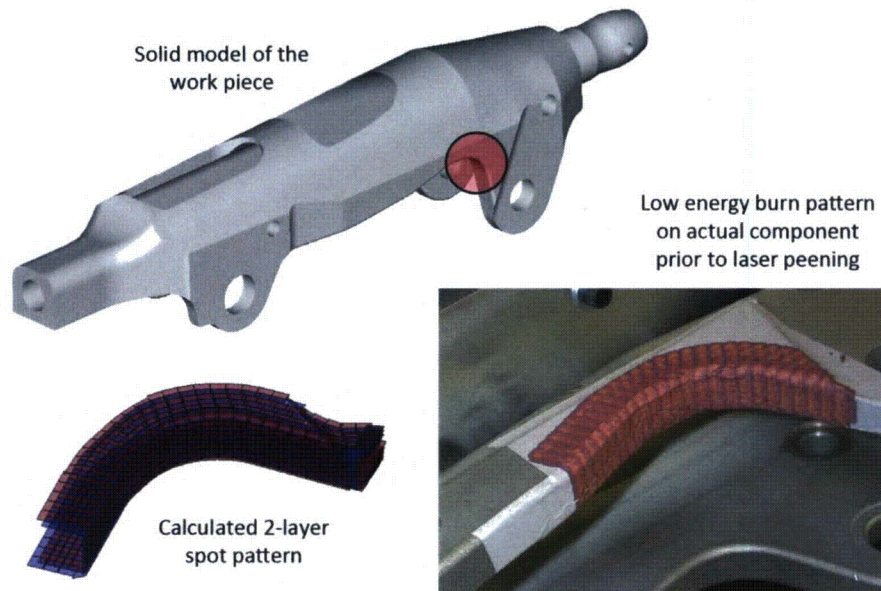


Figure 2-30
Square spots allow complex surfaces on the work piece to be air laser peened with precisely controlled spot-to-spot overlap, provided by MIC

2.4.4.1.4 *Laser beam quality*

The MIC laser system generates a single-frequency, single-transverse-mode laser beam with very high wave front fidelity. This is achieved using a non-linear process called phase conjugation. A stimulated Brillouin scattering (SBS) mirror corrects distortions in the laser system introduced by thermal gradients in the amplifier as well as by small fabrication errors in all of the optical components. It also corrects tilt errors in the amplifier, ensuring that the output beam maintains precisely the same pointing direction as it emerges from the laser. These functions are performed without sensors, computers, or actively adjusted optical elements.

The high beam quality eliminates the need to warm-up the laser system or to maintain a constant pulse repetition frequency. The first pulse from the laser has the same fidelity (spot shape and uniformity) as all subsequent pulses, providing a high degree of repeatability to the ALP process. The high beam quality also makes it possible to reliably transport the beam over long distances in cases where it is required for an air laser peening application at a customer site.

2.4.4.2 Transportable laser

The MIC laser system is packaged into a trailer as a part of a transportable laser peening system. This self-contained unit can be placed at a customer site and activated without the need for extensive configuration and set up. It only needs to be supplied with a standard 480VAC 3-phase power source and a one gpm source of tap water. The trailer is self-stabilizing using a built-in hydraulic leg system. It houses a clean room area for the laser system along with power, cooling, and computer controls. It also contains the water de-ionization for the air laser peening tamping layer. Figure 2-31 shows an example of one of the multiple transportable systems currently operated by MIC.

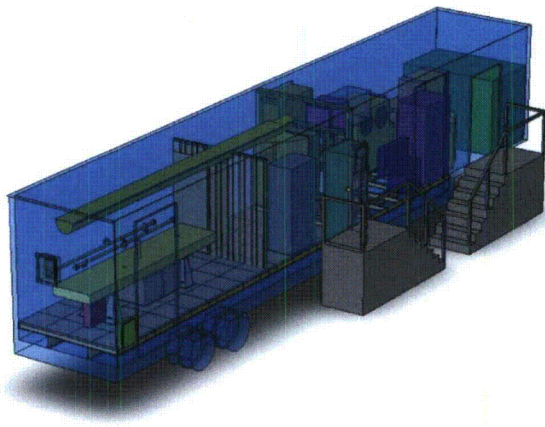


Figure 2-31

The MIC transportable air laser peening system: the figure on the left shows a schematic representation and the photo on the right shows a system in transit to Palmdale, CA to support on-site laser peening of F-22 aircraft, provided by MIC

2.4.4.3 Beam transport

Given the energy level of the MIC laser system, the beam is delivered by either air or vacuum propagation through stainless steel pipes between the laser trailer and the air laser peening processing area. Pathways through the customer facility can be accommodated by mirror boxes that are installed between sections of the pipe to allow direction changes. Portions of the beam transport system contain lenses to re-image the beam during transit and control diffraction, and the space between the lenses is evacuated to prevent air breakdown from the high laser intensity at focus. As discussed in Section 5.4.3, the existing beam transport system can be readily adapted to nuclear power plant applications.

2.4.4.4 Scanning beam delivery head

MIC has extensive experience in laser peening large, stationary work pieces that include 65' fighter aircraft and 105' long wing panels for passenger airplanes. Both of these are in full commercial production. The delivery of the laser beam to large parts requires methods of accurately aligning a treatment pattern and scanning the beam in order to place laser spots over

large areas of the work piece. Specialized optical tooling has been developed to perform these tasks.

The MIC beam scanning approach is based on a robotically manipulated beam delivery tool referred to as the stinger. Figure 2-32 shows an example of the stinger beam delivery system as currently in use on large aircraft. The high energy laser beam is fed to this tool across a free-air propagation path using a high-speed gimbal-mounted mirror, referred to as the transmitter gimbal, and received on the stinger by another mirror called the receiver gimbal. The stinger has the ability to direct the beam across a complex geometry on the work piece, placing a uniform pattern of spots across the laser peening treatment area. The beam is automatically adjusted for each spot, changing its divergence angle, beam rotation, polarization rotation, and aspect ratio to apply a uniform square spot, regardless of incidence angle onto the target surface. This allows a pattern of spots to be applied while keeping the stinger stationary. The wide field of view of the stinger allows multiple locations on the work piece to be peened without relocating the stinger. By laser peening from a collection of fixed stinger locations, line-of-sight obstructions can be avoided.

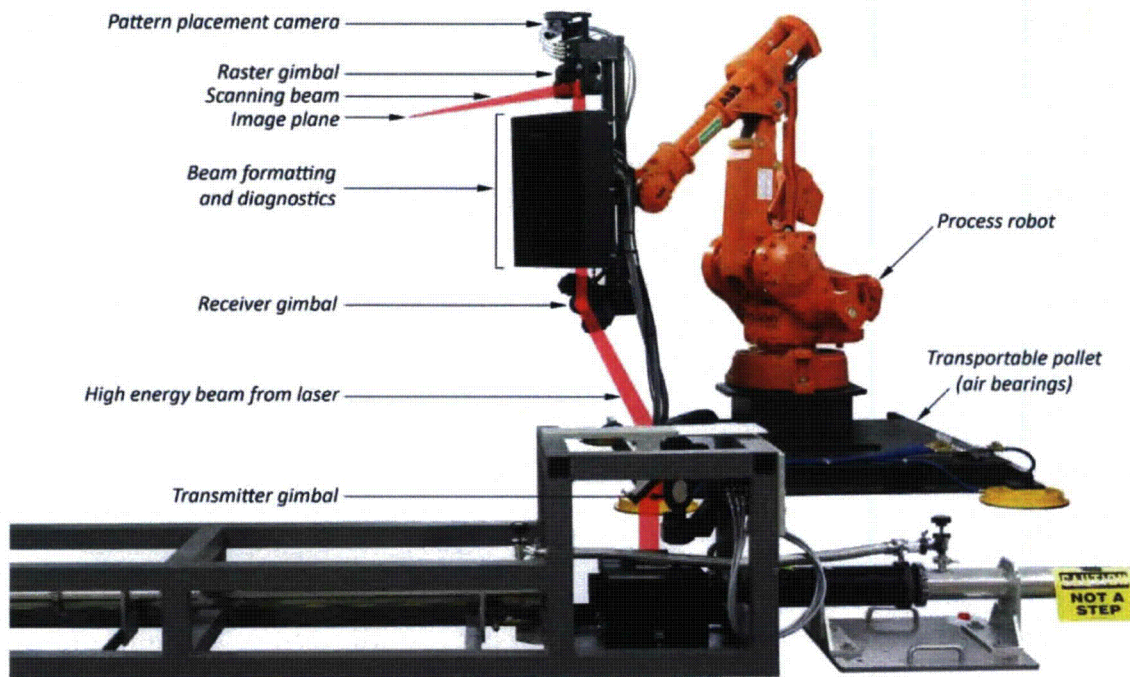


Figure 2-32
Photo showing the MIC air laser peening stinger design which allows spot patterns to be placed over complex features of a stationary work piece, provided by MIC

2.4.4.5 Pattern registration

A continuous-wave (CW, non-pulsed) low power tracer beam is superimposed on the same propagation path as the high energy beam and is used to maintain closed-loop alignment of the beam delivery optics, from the output of the laser trailer to the stinger. Since the tracer beam is

precisely co-aligned with the pulse beam, it can be used to calibrate the laser output to geometric features on the work piece. The beam delivery stinger has an integrated camera system that allows the tracer beam to be aligned to features of known locations. Approaches including photogrammetry and/or laser range finding then allow a virtual representation of the work piece in the coordinate system of the stinger to be built during processing, and patterns of laser peening spots to be accurately aligned onto the treatment surfaces.

2.5 Summary

The principles underlying three surface stress improvement techniques, ULP, ALP and WJP, are discussed in this section with respect to their functionality against PWSCC. The theoretical analysis and experimental results are compared for ULP to illustrate its effectiveness in developing surface compressive stresses in PWR materials. Due to the physical complexity of the generation of shock waves from cavitation bubble collapse during water jet peening, most of the key parameters of the WJP process, including acoustic shock wave pressure, are identified through experimental methods. The ULP and WJP methods typically result in a compressive residual stress layer that is roughly 1 millimeter (0.04 in.) deep. Because of its relatively high power laser source, the ALP process is capable of inducing deeper compressive residual stress layers, up to several millimeters deep. The experimental results in Section 2 and Section A.1 of Appendix A have demonstrated the functionality of underwater laser peening, water jet peening, and air laser peening at developing PWSCC inhibiting compressive stress fields in the surfaces of the Alloy 600/82/182 nickel-based materials, as well as stainless steel materials, used in PWRs.